

1
2
3
4
5
6
7
8
9
10
11
12
13
14
15
16
17
18
19
20
21
22

Revision 2

Trace element and isotopic (S, Pb) constraints on the formation of the giant Chalukou porphyry Mo deposit, NE China

Word Count: 11904

Qingqing Zhao¹, Degao Zhai^{1, 2*}, Anthony E. Williams-Jones², Jiajun Liu¹

¹*State Key Laboratory of Geological Processes and Mineral Resources, and School of
Earth Sciences and Resources, China University of Geosciences, Beijing, 100083,
China*

²*Department of Earth and Planetary Sciences, McGill University, Quebec, 3450,
Canada*

*E-mail: dgzhai@cugb.edu.cn

Revised submission to: *American Mineralogist*

With 13 Figures and 4 Tables

30-Dec-2021

23

ABSTRACT

24 Porphyry type Mo deposits have supplied most of the Mo to the world. However,
25 the source of the Mo and the controls on its enrichment in such deposits is still a
26 matter of great debate. In this study, we present in situ trace element and isotopic data
27 for a giant porphyry Mo deposit (the Chalukou Mo deposit in NE China) and use
28 these data to address these issues. Three primary paragenetic stages of mineralization
29 were recognized at Chalukou: (I) K-feldspar + quartz + minor pyrite (Py-I) + minor
30 molybdenite (Mol-I); (II) quartz + sericite + molybdenite (Mol-II) + pyrite (Py-II);
31 (III) quartz + chlorite + epidote + fluorite + pyrite (Py-III) + galena + sphalerite +
32 minor chalcopyrite. The bulk of the molybdenite was deposited in Stage II. In situ S
33 isotope analyses of the sulfide ores show that the $\delta^{34}\text{S}$ values vary from -5.2 to +7.8‰
34 (mean = +2.9‰), and correspond to $\delta^{34}\text{S}_{\text{H}_2\text{S}}$ values from -2.4 to +3.3‰ (mean =
35 +1.1‰). These values are consistent with a magmatic source for the sulfur. In situ Pb
36 isotope compositions of the sulfide ores are almost identical to those of the local
37 Mesozoic granites and other magmatic-hydrothermal ore deposits in this region,
38 suggesting a close genetic association between the Mo mineralization and felsic
39 magmatism.

40 Pyrite from the three stages of mineralization differs significantly in its trace
41 element composition. The first generation, Py-I, has a high Cu content (8.7 ± 49.6
42 ppm; where the first value is the median and the second is the standard deviation) and
43 Mo content (6.9 ± 3.8 ppm). Pyrite-II has the lowest Cu concentration (1.3 ± 2.1 ppm)
44 and a relatively high Mo concentration (5 ± 128 ppm), and Py-III has a high Cu

45 content (8.7 ± 37.1 ppm) but the lowest Mo content (0.05 ± 5.7 ppm). From this, we
46 infer that pyrite recorded the chemical evolution in the Mo/Cu ratio of the ore fluid,
47 and that this ratio reached a maximum in Stage II, coinciding with the widespread
48 saturation of the fluid in molybdenite. The evolution of the Mo/Cu ratio in pyrite
49 implies that the fluid was undersaturated in chalcopyrite at the high temperature of
50 Stage I, despite the Cu concentration of the fluid apparently being at its high level,
51 and chalcopyrite only saturated later, at lower temperature. Molybdenite, however,
52 because of its lower solubility, saturated early (Stage I), and in the subsequent stage
53 (Stage II) was supersaturated in the fluid.

54 There is a significant enrichment of Mo in the syn-ore intrusions at Chalukou
55 compared to the pre-ore monzogranite. The very low Sr/Y ratios for the Chalukou
56 syn-ore intrusions, which are in sharp contrast to the high Sr/Y ratios of the pre-ore
57 monzogranite and those of porphyries related to Cu deposits, suggest that fractional
58 crystallization of plagioclase may have been a key factor in generating the syn-ore
59 magmas. Molybdenum is a highly incompatible metal and will concentrate in the
60 crust, and assimilation of old continental crust, therefore, may explain the Mo
61 enrichment of the syn-ore intrusions and ultimately the formation of the giant
62 Chalukou deposit.

63 **Keywords:** Sulfur and lead isotopes, trace element chemistry, porphyry Mo deposits,
64 magma and fluid evolution, metal source and enrichment

65

66

INTRODUCTION

67 The genesis of porphyry type deposits has been a subject of debate since their
68 discovery ([Camus 1975](#); [Carten et al. 1988](#); [Clark et al. 1990](#); [Mathur et al. 2000](#);
69 [Sillitoe 2010](#); [Richards 2003, 2011](#); [Lee and Tang 2020](#)). Much of this debate has
70 centered on the sources of the ore metals and the processes of enrichment, particularly
71 for the giant deposits ([Audétat et al. 2000](#); [Chiaradia 2013](#); [Lee et al. 2012](#); [Chang et
72 al. 2018](#); [McFall et al., 2019](#)). Early models for the formation of porphyry deposits
73 focused on processes relating to subduction ([Clark et al. 1990](#); [Blevin 2002](#); [Richards
74 2003, 2011](#); [Olson et al. 2017](#)), but as some porphyry deposits form in post-collisional
75 settings, it has become clear that their genesis needs to be viewed through a wider lens
76 ([Hou et al. 2015](#); [Yang et al. 2015](#); [Yang and Cooke 2019](#); [Xu et al. 2021](#)). Whether
77 porphyry-type deposits emplaced in different tectonic settings have different metal
78 sources is a point of contention ([Zheng et al. 2019](#)). Some studies of porphyry Cu
79 deposits have suggested that the Cu is derived from a mixture of oceanic crust and
80 mantle during subduction ([Zhou et al. 2015](#)). Others have concluded that, in arc
81 magmas, there is a negative correlation between crustal thickness and copper content
82 ([Chiaradia 2013](#)), which suggests that the required Cu may come from the deep
83 continental crust ([Sillitoe 2010](#)). It is thought, however, that in the unusually
84 well-endowed Colorado and Qinling Mo porphyry districts a large proportion of the
85 molybdenum came from recycling of ancient continental crust ([Carten et al. 1993](#);
86 [Mao et al. 2011](#)).

87 The Great Hingan Range metallogenic belt, which lies in the eastern part of the
88 Central Asian orogenic belt (CAOB), hosts numerous porphyry Mo (-Cu), skarn Fe,

89 epithermal Au-Ag and polymetallic (Ag-Pb-Zn) vein deposits ([Chen et al. 2012, 2017](#);
90 [Zhai et al. 2014, 2017, 2019, 2020](#); [Shu et al. 2016](#); [Gao et al. 2016](#); [Xing et al. 2020](#)).
91 More than 80 Mo deposits have been discovered in northeast China (e.g., [Chen et al.](#)
92 [2017](#); [Xing et al. 2020](#)), and among them, the Chalukou deposit is the largest
93 (reserves of 2.46 Mt @ 0.087 wt.% Mo; [Zhao et al. 2021a](#)). Previous studies have
94 discussed the deposit geology and its tectonic setting ([Jin et al. 2014](#)), the age of the
95 mineralization ([Nie et al. 2011](#); [Liu et al. 2014b](#); [Zhang and Li 2017](#); [Zhao et al.](#)
96 [2021a](#)), the bulk rock geochemical and Sr-Nd-Hf isotope compositions ([Li et al. 2014](#);
97 [Liu et al. 2015a](#); [Liu et al. 2017](#); [Duan et al. 2018](#)), the fluid inclusion characteristics
98 and the H-O-S-Pb isotope data ([Liu et al. 2014a](#); [Li et al. 2019](#)). These studies have
99 concluded that the Chalukou deposit was the product of hydrothermal processes
100 related to a set of highly-fractionated magmatic rocks, including monzogranite,
101 granite porphyry, fine-grained porphyry and quartz porphyry, during the subduction of
102 the Mongol-Okhotsk Ocean ([Nie et al. 2011](#); [Li et al. 2014](#); [Liu et al. 2017](#)). Issues
103 relating to metal source and the processes of metal enrichment, however, have not
104 been fully addressed. Whether the Mo was supplied by old continental crust, as in the
105 Colorado and Qinling metallogenic belts, or a thickened lower crust enriched by
106 intracrustal magmatic processes in a subduction zone remains unresolved.

107 In this paper, we report results of a detailed study of the in situ trace element and
108 sulfur and lead isotopic composition of three generations of pyrite and molybdenite in
109 the Chalukou Mo deposit, and use them to determine the metal source, reconstruct
110 aspects of the fluid evolution and gain insight into the Mo enrichment process. The

111 new results indicate that in situ compositional (including isotopes and trace elements)
112 analyses of sulfides can provide valuable information on the environment of origin
113 and chemical evolution (including metal ratios) of the ore fluid.

114 **REGIONAL GEOLOGY**

115 The Chalukou porphyry Mo deposit is located in the Heilongjiang province in NE
116 China, and occurs within the Great Hingan Range metallogenic belt, which lies in the
117 eastern part of the CAOB ([Fig. 1A](#)). More than 80 Mo deposits have been discovered
118 in this area, with a combined reserve of 11.4 Mt Mo, making NE China one of the
119 World's most important Mo metallogenic provinces ([Chen et al. 2017](#); [Xing et al.](#)
120 [2020](#); [Shu and Chiaradia 2021](#)).

121 The rocks exposed in the vicinity of the Chalukou deposit comprise a Precambrian
122 basement, Paleozoic volcanic-sedimentary sequences and Mesozoic volcanic rocks
123 ([Fig. 1B](#); [Liu et al. 2017](#)). The Precambrian basement has been subdivided into the
124 Xinghuadukou Group and Dawangzi Formation, with the former being composed of
125 migmatite, granulite, biotite-plagioclase gneiss, two-mica schist and marble. Zircon
126 U-Pb analyses provide an age of about 850 Ma for the Xinghuadukou group ([Ge et al.](#)
127 [2015](#)). This suite is overlain unconformably by greenschist facies quartz-chlorite
128 schist, quartz-biotite schist and minor marble of the Dawangzi Formation ([Zhou et al.](#)
129 [2011](#); [Liu et al. 2017](#)). The Paleozoic volcano-sedimentary sequences comprise the
130 early Ordovician Tongshan and Duobaoshan Formations and the Devonian to early
131 Carboniferous Niquihe, Hongshuiquan and Baoligaomiao Formations ([Li et al. 2018](#)).

132 The Ordovician formations consist dominantly of tuffaceous sandstone, siltstone,
133 limestone, andesite, dacite, tuff, minor marble and slate, and were deposited between
134 490 and 470 Ma (Li et al. 2018). These rocks occur mainly in the eastern Hingan
135 Massif. The Devonian to early Carboniferous sedimentary sequences, which mainly
136 comprise sandstone, bioclastic limestone, shale and slate (Wu et al. 2015; Liu et al.
137 2017), are widely distributed from the Erguna block to the Hingan Massif. They are
138 overlain by Mesozoic volcanic rocks composed mainly of andesite, rhyolitic tuff and
139 rhyolitic pyroclastic rocks that are widespread in the region (Fig. 1B).

140 Northeast China is composed of several micro-blocks (Fig. 1B; Chen et al. 2017),
141 i.e., the Erguna, Hingan, Songliao, Lesser Hingan, and Jiamusi blocks. Multiple
142 subduction and collisional events involving these blocks resulted in widespread
143 magmatism (Chen et al. 2017). The Paleo-Asia Ocean that existed between the North
144 China Craton and the Siberian Craton finally closed in the late Permian-early Triassic,
145 leading to the assembly of several microcontinental blocks, i.e., the Lesser Hingan,
146 Jiamusi and Songliao blocks (Johnson et al. 2001; Zeng et al. 2013; Zhao et al. 2021b),
147 and the emplacement of numerous I-type granitoids (Zorin et al. 2001; Chen et al.
148 2017). The first episode of Mo mineralization in this region was during this period,
149 e.g., the emplacement of the Gaogangshan (~250 Ma, Zhang et al. 2017) and
150 Bilugangan (~237 Ma, Tang et al. 2012) porphyry Mo deposits.

151 After the closure of the Paleo-Asia Ocean, NE China gradually transformed into a
152 syn- to post-collisional extensional setting, characterized by the widespread
153 occurrence of Mesozoic S-type granitoids (Jahson et al. 2001; Wu et al. 2011). The

154 second episode of regional Mo mineralization occurred at this time, and is
155 exemplified by the Wudaoling skarn (~194 Ma, [Shi et al. 2012](#)) and Luming porphyry
156 Mo deposit (~177 Ma, [Chen et al. 2017](#)). This was followed by the south to
157 southeastward subduction of the Mongol-Okhotsk oceanic plate at ~165 Ma ([Wang et](#)
158 [al. 2017](#)), which eventually led to the closure of the Mongol-Okhotsk Ocean, the
159 timing of which is still unresolved ([Chen et al. 2017](#)). Some researchers consider that
160 the Mongol-Okhotsk Ocean was closed in a scissor-like style from west to east
161 between the mid-Jurassic and early Cretaceous ([Fritzell et al. 2016](#); [Chen et al. 2017](#)),
162 and associate this closure with the third regional Mo mineralization event (e.g.,
163 Chalukou, ~147 Ma, [Nie et al. 2011](#), Caosiyao, ~148 Ma, [Wang et al. 2017](#)). Other
164 researchers, however, consider the third Mo mineralization event to be a product of
165 the westward subduction of the Paleo-Pacific oceanic plate ([Chen et al. 2017 and](#)
166 [references therein](#)).

167 **ORE DEPOSIT GEOLOGY**

168 The Chalukou ore district is 8 km long and 5 km wide, and is divided into the
169 eastern and western exploration zones, which are separated by the Duobukuer River.
170 Exploration has focused mainly on the eastern exploration zone, where the main
171 molybdenum resource is located ([Nie et al. 2011](#)).

172 **Local rocks**

173 The tectonostratigraphic sequence exposed in the vicinity of the Chalukou deposit
174 comprises rocks ranging in age from Neoproterozoic to Mesozoic ([Fig. 2A](#); [Xiong et](#)

175 [al. 2015](#)). Neoproterozoic metamorphic rocks of the Dawangzi Formation crop out in
176 the center of the ore district and discontinuously to the northeast. These rocks
177 comprise quartz-chlorite schist, quartz-biotite schist, meta-sandstone, and minor
178 marble; a recent zircon U-Pb analysis of quartz-chlorite schist collected from this
179 formation yielded an age of 684.4 ± 9.5 Ma, which represents the formation age of the
180 protolith ([Li et al. 2018](#)). The main hosts to the ores are volcano-sedimentary rocks
181 that have been considered to be part of the thick, late Jurassic Guanghai Formation
182 ([Liu et al. 2015a](#)). They comprise tuffs of rhyolitic, dacitic and andesitic composition
183 and are particularly well-exposed in the eastern exploration zone where they have a
184 thickness of > 1500 m. Recent zircon U-Pb data for three drill core samples (rhyolite,
185 dacite and tuff) returned ages ranging from 473.9 ± 3.7 to 470.7 ± 2.4 Ma,
186 constraining their formation to the early Ordovician. These ages coincide with those
187 of the regional Duobaoshan Formation (from 490 Ma to 470 Ma, [Li et al. 2018](#)).
188 Widespread late Jurassic to early Cretaceous volcano-sedimentary rocks generated
189 from the eruption of the Jinsong caldera ([Li et al. 2014](#)), namely those of the
190 Baiyingaolao Formation, comprise andesite, dacite, rhyolite, breccia, tuff and lava;
191 the tuff breccia yielded a zircon U-Pb age of 135 ± 1 Ma ([Nie et al. 2011](#); [Liu et al.](#)
192 [2017](#)).

193 **Intrusions**

194 There were three episodes of intrusions in the Chalukou area, i.e., pre-, syn- and
195 post-ore intrusions, as revealed by detailed core logging and cross-cutting
196 relationships ([Fig. 2A, B](#); [Liu et al. 2014b](#)). The principal pre-ore intrusion is a

197 monzogranite, which is only observed in drill core at depths > 600 m below the
198 southeast part of the Chalukou deposit and crops out over an area of > 80 km² outside
199 the ore district (Fig. 2B). A zircon U-Pb radiometric determination yielded an age for
200 the monzogranite of 166 ± 2 Ma (Liu et al. 2014b; Zhao et al. 2021a).

201 The syn-ore intrusions comprise granite porphyry, quartz porphyry and fine-grained
202 porphyry. The granite porphyry occurs as apophyses or small stocks that intrude the
203 Ordovician volcano-sedimentary rocks and have widths ranging from 3 to 80 m. The
204 quartz porphyry was emplaced in the shallow parts of the deposit as small stocks
205 intruding the Ordovician volcano-sedimentary rocks (~100 m; Fig. 2B), and is
206 compositionally similar to the granite porphyry. A single fine-grained porphyry
207 intruded the Ordovician volcano-sedimentary rocks in the central part of the ore
208 district. This intrusion is only encountered at a depth >600 m (Fig. 2B). Based on
209 zircon U-Pb radiometric determinations, the granite porphyry, quartz porphyry, and
210 fine-grained porphyry are coeval with ages of 152.1 ± 2.2 , 148.2 ± 2.2 , and $148.1 \pm$
211 2.6 Ma, respectively (Li et al. 2014, Liu et al. 2014b; Zhang and Li 2017; Duan et al.
212 2018, Zhao et al. 2021a).

213 The post-ore intrusions comprise diorite porphyry and quartz monzonite porphyry,
214 and occur mainly as small dikes (Fig. 2B) that cross-cut the earlier intrusions as well
215 as the Mo orebodies (Li et al. 2014). Zircon from the diorite porphyry and quartz
216 monzonite porphyry yielded U-Pb ages of 132.7 ± 2.5 and 128.4 ± 2.1 Ma,
217 respectively (Li et al. 2014; Liu et al. 2017).

218 **Alteration and mineralization types**

219 The various rock-types exposed in the mine area, including quartz-chlorite schist of
220 the Dawangzi Formation, volcano-sedimentary rocks of the Ordovician Duobaoshan
221 Formation and the Jurassic monzogranite, all experienced intense hydrothermal
222 alteration related to the emplacement of the syn-ore intrusions (granite porphyry,
223 quartz porphyry and fine-grained porphyry). An elliptical alteration zone with a long
224 axis of ~1800 m and a short axis of 400-800 m is observed on the surface, and is
225 characterized by a central silicic core that passes outwards through potassic, phyllic
226 and argillic alteration to propylitic alteration (Fig. 2C; Li et al. 2019). Potassic and
227 phyllic alteration are closely associated with Mo mineralization. Silicification is
228 restricted to the apex of the fine-grained porphyry, where it is spatially associated
229 with unidirectional solidification textures (UST). Only minor disseminated or veinlet
230 Mo mineralization could be observed in this zone (Fig. 3A, B). Potassic alteration
231 developed along the contact between the fine-grained porphyry and Ordovician
232 volcano-sedimentary rocks, and/or between the granite porphyry and Ordovician
233 volcano-sedimentary rocks at depths of >400 m (Jin et al. 2014), in a zone that
234 reaches a width of 1200 m in cross-section. Mineralogically, this zone is identified by
235 the abundance of K-feldspar and quartz (Fig. 3 C, D; Nie et al. 2011; Jin et al. 2014).
236 Phyllic alteration is present mainly in the lower Ordovician volcano-sedimentary
237 rocks and overprinted the earlier potassic alteration (Fig. 3E). It forms a zone
238 measuring 1200 m in length, 300-400 m in width and ~800 m in depth (Liu et al.
239 2017). Phyllic alteration is characterized by the mineral assemblage, quartz + sericite

240 + fluorite + pyrite \pm molybdenite \pm calcite. Abundant sericite is observed as halos
241 (2-10 mm wide) along quartz veins. The argillic alteration is developed irregularly at
242 the margin of the phyllic zone (Liu et al. 2017) and consists of quartz, calcite and
243 pyrite with minor galena, sphalerite and chalcopyrite. Propylitic alteration is observed
244 mainly in the Dawangzi Formation, the lower Ordovician rocks and the monzogranite,
245 and is manifested by the assemblage epidote-chlorite-calcite.

246 The economic mineralization in the Chalukou deposit has been subdivided into a
247 lower Mo mineralized zone and an upper zone of Pb-Zn mineralization (Li et al. 2014;
248 Liu et al. 2014b; Duan et al. 2018). The Pb-Zn mineralization occurs as quartz-sulfide
249 veins in Ordovician volcano-sedimentary rocks and is associated with propylitic and
250 argillic alteration (Jin et al. 2014). This mineralization constitutes a resource of 0.143
251 Mt Pb @ 0.6 wt.% and 0.013 Mt Zn @ 0.3 wt.% (Liu et al. 2017; Duan et al. 2018).
252 The Pb-Zn mineralized veins vary in width from 0.2 to 2 m, occur above the Mo
253 orebodies and locally cross-cut the Mo-bearing veins, indicating a relatively late
254 timing of emplacement (Liu et al. 2014b). The Mo mineralization, most of which
255 occurs as stockwork or veins (Figs. 3 and 4 A-C), is hosted by fine-grained porphyry,
256 granite porphyry, breccia pipes and lower Ordovician volcano-sedimentary rocks. It is
257 zoned vertically in terms of grade from a thin, low-grade (<0.06 wt.% Mo) domain in
258 the upper part of the deposit through a thicker, medium-grade (0.06-0.26 wt.% Mo)
259 intermediate domain, to a thick, high-grade (0.08-0.53 wt.% Mo) domain in the lower
260 part of the deposit (Fig. 2D; Nie et al. 2011; Zhang and Li 2017).

261 **Mineralization stages**

262 The ore minerals in the Chalukou deposit comprise molybdenite, pyrite and minor
263 sphalerite, galena, chalcopyrite and hematite, and the main gangue minerals are quartz,
264 K-feldspar, plagioclase, sericite, fluorite, calcite, epidote and chlorite. Based on
265 cross-cutting relationships among the different vein-types, and the mineral
266 assemblages, the Chalukou mineralization has been subdivided into three ore stages.

267 Stage I mineralization consists of quartz veins and minor disseminated
268 mineralization and is represented by the mineral assemblage quartz + K-feldspar +
269 minor pyrite + minor molybdenite \pm magnetite \pm hematite \pm fluorite. The veins (0.5-2
270 mm) in this stage generally have halos of strong silicification or potassic alteration.
271 Numerous quartz veinlets are observed to cross-cut the USTs that are associated with
272 this stage (Zhao et al. 2021a). Magnetite occurs as subhedral to euhedral grains with
273 obvious growth zones and was replaced by hematite (martite) (Fig. 4D, E). The
274 magnetite and hematite occur as veinlets (Liu et al. 2015a) or irregularly shaped
275 masses in association with quartz. The vein-hosted and disseminated molybdenite
276 (Mol-I) of Stage I occurs as euhedral plate-like crystals (Fig. 5A, B) in potassically
277 altered granite porphyry. The pyrite (Py-I) is in the form of subhedral to euhedral
278 crystals (Figs. 4F, G and 5A, B), and is generally cross-cut and replaced by later
279 molybdenite (Mol-II, Fig. 4F).

280 The main ore stage (Stage II) is composed of mineralized veins and breccias, which
281 contain molybdenite and minor pyrite, accompanied by quartz, K-feldspar, sericite
282 and fluorite. Veins (0.2-5 cm) in this stage can be subdivided into quartz +
283 molybdenite \pm fluorite, quartz + K-feldspar + molybdenite (Fig. 3C), quartz + sericite

284 + molybdenite ± pyrite and molybdenite-dominant types. Molybdenite (Mol-II)
285 usually occurs along the edges of the quartz + K-feldspar veins, and locally delineates
286 a suture in the vein-center (Fig. 5A, B). These veins are surrounded by sericite halos.
287 In some cases, the vein consists dominantly of molybdenite and contains only minor
288 quartz (Zhao et al. 2021a). The major modes of occurrence of Mol-II are as
289 fine-grained aggregates (Figs. 4F and 5D) and wispy lamellae (Fig. 5 E-G) that vary
290 from 20 to 250 μm in width and 50 to 500 μm in length. These aggregates are
291 associated with pyrite (Py-II), which is coarse-grained, cross-cuts Mol-II or contains
292 inclusions of Mol-II (Fig. 4H).

293 Stage III veins are composed of quartz, pyrite, galena, sphalerite, chlorite, epidote,
294 fluorite and minor chalcopyrite. Pyrite (Py-III) is coarse-grained and is associated
295 with quartz, galena, sphalerite, and fluorite (Fig. 4B, C, J, K). Chalcopyrite is rarely
296 observed and occurs only as inclusions in sphalerite (Fig. 4I). It may also coexist with
297 galena and/or sphalerite and was replaced by pyrite (Liu et al. 2015a). Galena and
298 sphalerite occur at the margins of pyrite crystals (Fig. 4J).

299 **SAMPLES AND ANALYTICAL METHODS**

300 **In situ trace element analyses**

301 The trace element concentrations of pyrite and molybdenite were analyzed in situ
302 using an Agilent 7500a ICP-MS, equipped with a New Wave 193 nm laser at the State
303 Key Laboratory of Geological Processes and Mineral Resources, China University of
304 Geosciences, Beijing. The laser ablation included a pre-ablation period of 5 s to clean

305 the surface of the samples, 20 s for background measurement, and 45 s for signal
306 collection. The repetition rate of the laser was 10 Hz and the spot diameter was 36 μm .
307 The external standard NIST 610 was used for calibration, NIST 612 was used as the
308 monitoring standard and MASS-1 was used as a blind sample. The integration time
309 was 8 ms for ^{57}Fe , ^{63}Cu , ^{66}Zn , 15 ms for ^{51}V , ^{55}Mn , ^{59}Co , ^{60}Ni , ^{71}Ga , 20 ms for ^{82}Se ,
310 ^{111}Cd , ^{115}In , ^{116}Sn , ^{121}Sb , ^{205}Tl , ^{209}Bi , 30 ms for ^{75}As , ^{95}Mo , ^{182}W , ^{208}Pb , ^{238}U , and 80
311 ms for ^{107}Ag , ^{197}Au and other elements. Details of the analytical method can be found
312 in Zhang et al. (2019).

313 **In situ sulfur and lead isotope analyses**

314 In situ sulfur and lead isotopic analyses of sulfides (molybdenite, pyrite, galena and
315 sphalerite) were carried out at the State Key Laboratory of Continental Dynamics,
316 Northwest University, China. Detailed descriptions of the methods employed in the
317 analyses can be found in Yuan et al. (2017). The sulfur isotopic measurements were
318 made using a Nu Plasma 1700 MC-ICP-MS (Nu instruments, UK) coupled to a
319 RESOLUTION M-50 laser ablation system (ASI, Australia) equipped with a 193 nm ArF
320 CompexPro102 excimer laser (Coherent, USA). A spot size of 37 μm was adopted
321 with a laser repetition rate of 3-4 Hz and an energy density of 3.5-4.0 J/cm^2 . Each
322 sample acquisition consisted of background collection for 30 s, followed by ablation
323 signal collection for 50 s. A standard-sample bracketing method was used to correct
324 the mass discrimination and instrumental drift. The external standards for sphalerite,
325 pyrite and galena were NIST NBS123, PY-4, and CBI-3, respectively. The analytical
326 precision calculated from replicate analyses of unknown samples was better than 0.2‰

327 (1 σ). In situ lead isotopic analyses were conducted with a Nu Plasma II MC-ICP-MS
328 instrument (Nu Instruments, UK) coupled to a 266 nm NWR UP Femto laser ablation
329 system (ESI, USA). The laser ablation employed a spot size of 15 μm for galena and
330 50 μm for pyrite and molybdenite, a maximum energy density of 6 J/cm², and a laser
331 frequency of 5-50 Hz. A NIST SRM 997 Tl dry aerosol (50 ng/g, ²⁰⁵Tl/²⁰³Tl = 2.3889)
332 standard was used in conjunction with the standard-sample bracketing method to
333 correct for the mass discrimination of the mass spectrometer. Repeated analyses of the
334 NIST SRM 610 glass standard yielded reproducible results with mean ²⁰⁶Pb/²⁰⁴Pb,
335 ²⁰⁷Pb/²⁰⁴Pb and ²⁰⁸Pb/²⁰⁴Pb ratios of 17.052 \pm 0.003, 15.515 \pm 0.003 and 36.980 \pm
336 0.007 (1 σ , n = 183), respectively.

337 **Whole-rock lead isotope analyses**

338 Whole-rock lead isotope analyses of the intrusive rocks were conducted at the
339 Beijing Research Institute of Uranium Geology, China National Nuclear Corporation.
340 The samples were cleaned in deionized water and leached in hot 6 N HCl for 15 to 20
341 minutes. Then, the samples were dissolved using HF and HClO₄, and treated with a
342 basic anion exchange resin to purify Pb. The Pb isotopes were measured by thermal
343 ionization mass spectrometry using a mass spectrometer (Thermo Finnigan); the
344 measurement accuracy was better than 0.005%. The measured Pb isotope ratios of the
345 Pb standard reference NBS 981 were ²⁰⁶Pb/²⁰⁴Pb = 16.937 \pm 0.002, ²⁰⁷Pb/²⁰⁴Pb =
346 15.457 \pm 0.002 and ²⁰⁸Pb/²⁰⁴Pb = 36.611 \pm 0.004, respectively, and are consistent with
347 the reference values (Todt et al. 1993).

348

RESULTS

349 Trace elements

350 Molybdenite samples from the Chalukou deposit have highly variable trace element
351 concentrations (Table 1; Fig. 6). However, the concentrations are generally lower in
352 Mol-I than in Mol-II (Fig. 6). The median concentrations of V, Cu, Zn, Ag, Sb, and W
353 in Mol-I are < 10 ppm, but the concentrations of some of these metals can range to
354 very high values, e.g., Zn (1250 ppm) (Table 1; Fig. 6), due to the presence of
355 sub-microscopic inclusions. Compared to Mol-I, Mol-II is enriched in almost all the
356 metals analyzed and the median concentrations of V, Cu, Zn, Ag, Sb and W in Mol-II
357 are all over 10 ppm. The median content of Ti in Mol-II is 312 ppm. There is a strong
358 correlation of Ti with Fe. Analysis of some Mol-II crystals yielded anomalously high
359 Ti contents (Fig. 7A), due probably to the presence of submicroscopic ilmenite and/or
360 rutile inclusions.

361 Both Mol-I and Mol-II have high concentrations of Fe and Pb with median values
362 of 894, 7570 ppm and 269, 4519 ppm, respectively (Table 1). The Co and Ni contents
363 of Mol-I and Mol-II are relatively low, with median values of 0.2, 1.9 ppm and 3.8,
364 4.4 ppm, respectively. Though Mol-II contains slightly more Co and Ni than Mol-I,
365 both have a Co/Ni ratio <1. There are strong correlations (Fig. 7 B-E) between Fe and
366 Cu ($R^2 = 0.77$), Bi and Pb ($R^2 = 0.97$), Bi and Ag ($R^2 = 0.74$), W and As ($R^2 = 0.73$),
367 and a weak correlation between Sb and Au ($R^2 = 0.35$; Fig. 7F).

368 Trace element concentrations in pyrite are variable and lower than in molybdenite

369 (Table 1; Figs. 8, 9). There is a progressive decrease in the contents of Ti, Mn, Zn, Cd,
370 Sn and W from Py-I through Py-II, to Py-III (Fig. 8). The Cu content decreases from a
371 median of 8.7 ppm in Py-I, to a median of 1.3 ppm in Py-II but increases in Py-III to a
372 median of 8.7 ppm. The Py-I samples have the highest Mo contents (6.9 ± 3.8 ppm,
373 where the first value is the median and the second value is the standard deviation,
374 S.D.; Table 1). The Py-II samples have a relatively high Mo content (5.0 ± 128.1 ppm)
375 and the lowest Cu content (1.3 ± 2.1 ppm) of the three pyrite types, whereas the Py-III
376 sample is generally enriched in Cu (8.7 ± 37.1 ppm) and extremely depleted in Mo
377 (0.05 ± 5.7 ppm) (Table 1; Fig. 8).

378 There are good correlations among Pb, Ag and Bi (Fig. 9A, B) and weaker
379 correlations among Zn, Ti and Mn (Fig. 9C, D). Most elements (e.g., As, Co, Ni and
380 Se, Fig. 10A) show relatively smooth curves in the time-resolved depth profiles. For
381 Pb, Ag and Bi, the spikes could be found in the time-resolved depth profiles of sample
382 C142Q2-3 (Fig. 10B). Samples of Py-I and Py-II have relatively high Co (median
383 values of 12 and 10 ppm, respectively) and Ni (median values of 19 and 5 ppm,
384 respectively) concentrations, and Co/Ni ratios ranging between 0.04 and 7.71 (Fig.
385 9E). The Py-III samples, however, have much lower Co (median = 0.2 ppm) and Ni
386 (median = 0.6 ppm) contents than Py-I and Py-II, and the Co/Ni ratios are all < 1 (Fig.
387 9E).

388 Sulfur and lead isotope ratios

389 The results of the in situ sulfur isotope analyses are reported in Table 2 and

390 illustrated in [Figure 11A](#). The full dataset has $\delta^{34}\text{S}_{\text{V-CDT}}$ values in the range from -5.2
391 to +7.8‰; the mean is +2.9‰. The molybdenite is characterized by relatively high
392 $\delta^{34}\text{S}$ values (+4.2 to +7.8‰) compared to the other sulfides. The 17 spots for Py-I,
393 Py-II and Py-III all yielded similar values, which range from +3.2 to +4.2‰ (mean =
394 3.7‰), +1.4 to +2.5‰ (mean = 2.1‰) and +1.1 to +4.6‰ (mean = 3.0‰),
395 respectively. Within single pyrite crystals, there is a small but significant $\delta^{34}\text{S}$
396 variation from +1.1 to +3.3‰; the cores have typically ~2‰ isotopically heavier
397 values than mantles ([Fig. 11A](#)). The sphalerite yielded $\delta^{34}\text{S}$ values of +0.2 to +2.4‰.
398 Two spots for galena returned $\delta^{34}\text{S}$ values of -5.2 and -5.0‰.

399 The lead isotope compositions of the sulfides are reported in [Table 3](#) and illustrated
400 in [Figure 12](#). The $^{206}\text{Pb}/^{204}\text{Pb}$ ratios vary from 18.274 to 18.386, $^{207}\text{Pb}/^{204}\text{Pb}$ from
401 15.518 to 15.597, and $^{208}\text{Pb}/^{204}\text{Pb}$ from 38.097 to 38.308. Significantly, the sulfides
402 from Stages I and II (Mol-I, Mol-II, Py-I and Py-II) contain more radiogenic lead than
403 the Stage III sulfides (i.e., Py-III, galena and sphalerite).

404 **Whole-rock lead isotope ratios**

405 The whole rock Pb isotope compositions of the syn-ore (granite porphyry, quartz
406 porphyry and fine-grained porphyry) intrusions are similar, with $^{206}\text{Pb}/^{204}\text{Pb}$,
407 $^{207}\text{Pb}/^{204}\text{Pb}$, and $^{208}\text{Pb}/^{204}\text{Pb}$ values of 18.442-18.570, 15.549-15.591, and
408 38.323-38.482, respectively ([Table 4](#); [Fig. 12](#)). These values are also similar to those
409 of sulfides, especially the ratios of $^{207}\text{Pb}/^{204}\text{Pb}$, which completely overlap with sulfides
410 in the Chalukou deposit.

411

DISCUSSION

412 Sulfur and lead sources

413 **Sulfur sources.** As reported above, the sulfur isotope compositions of the Chalukou
414 sulfides have $\delta^{34}\text{S}$ values ranging from -5.2 to +7.8‰, which decrease in the order
415 molybdenite, pyrite, sphalerite and galena (Fig. 11A; Table 2). In order to calculate
416 the corresponding $\delta^{34}\text{S}$ for H_2S in equilibrium with each sulfide, we used the
417 homogenization temperatures of fluid inclusions from previous studies, which are 320
418 to 480 °C for the early quartz + K-feldspar stage, 260 to 410 °C for the
419 quartz-molybdenite stage, and 200 to 250 °C for the late
420 quartz-pyrite-galena-sphalerite stage (Liu et al. 2014a; Li et al. 2019). The
421 corresponding range and mean $\delta^{34}\text{S}_{\text{H}_2\text{S}}$ values of the different stages are from +2.3 to
422 +3.3‰ (mean = 2.8‰; T= 400°C) for Stage I, from +0.4 to +1.5‰ (mean = 1.1‰; T=
423 350°C) for Stage II, and from -2.7 to +2.8‰ (mean = 0.8‰; T= 225°C) for Stage III.
424 The narrow range of $\delta^{34}\text{S}_{\text{H}_2\text{S}}$ values centered on 0‰ (-2.7 to +3.3‰, mean = 1.0‰)
425 indicates a magmatic sulfur source (Seal 2006). However, the sulfur isotope
426 fractionation of over 6‰ between coexisting galena and sphalerite in Stage III implies
427 a temperature of 101 °C, which is much lower than the homogenization temperature
428 described above, indicating that the two minerals were not in isotopic equilibrium
429 (Seal 2006).

430 The $\delta^{34}\text{S}_{\text{H}_2\text{S}}$ values for Chalukou are similar to those reported for other
431 magmatic-hydrothermal ore deposits in the region (Appendix Table A1; Ma 1984;

432 Zhao et al. 2016), e.g., the Daheishan porphyry Mo deposit (-0.8 to +3.0‰; Hu et al.
433 2014), the Badaguan porphyry Cu-Mo deposit (-1.8 to +2.4‰; Mi et al. 2017; Hou
434 2014; Kang 2015; Gao et al. 2016), and the Wunugetushan porphyry Cu-Mo deposit
435 (-0.1 to +2.8‰; Chen et al. 2011; Zhang et al. 2016). All of these deposits are close to
436 the Derbugan fault, which is the boundary between the Erguna block and the Hingan
437 block and the locus of a large number of Mesozoic granites (Fig. 1B). In contrast,
438 $\delta^{34}\text{S}_{\text{H}_2\text{S}}$ values for deposits in the Duobaoshan ore district, which is located to the east
439 of the Derbugan fault area and characterized by widely distributed Paleozoic rocks
440 (Fig. 1B), are generally negative (Fig. 11B), e.g., the Zhengguang gold deposit (-14.2
441 to +1.6‰; Fu et al. 2014; Gao et al. 2017), the Tongshan Cu deposit (-1.1 to -0.2‰;
442 Liu et al. 2015b), the Sankuanggou skarn Fe-Cu deposit (-4.5 to -0.5‰; Deng et al.
443 2018), and the Duobaoshan porphyry Cu deposit (-3.2 to -0.5‰; Fu et al. 2014).
444 However, some deposits in the Duobaoshan ore district also have positive $\delta^{34}\text{S}_{\text{H}_2\text{S}}$
445 values, e.g., the Yongxin gold deposit (+2 to +3.9‰; Yuan et al. 2018).

446 The above observations indicate that there are differences in the sulfur isotope
447 composition of the fluids forming deposits close to the Derbugan fault and those in
448 the Duobaoshan ore district, although all the deposits in both regions are of
449 magmatic-hydrothermal origin. Moreover, the sulfur isotope values are independent
450 of the ore deposit type, and mineral paragenesis (Chen et al. 2011; Hu et al. 2014; Mi
451 et al. 2017; Yuan et al. 2018). Geologically, the two regions differ significantly.
452 Whereas Paleozoic sedimentary strata are common in the Duobaoshan district,
453 Mesozoic volcanics and granites are dominant in the Derbugan fault area (Fig. 1B).

454 Furthermore, sulfur isotope data for the Palaeozoic sedimentary rocks in this area
455 show that the $\delta^{34}\text{S}$ values range from -43.8 to -8.5‰ (mean = -35.48‰; [Huang et al.](#)
456 [2018](#)). We therefore infer that there was a considerable contribution of sulfur from the
457 Paleozoic strata in the Duobaoshan area, leading to negative $\delta^{34}\text{S}_{\text{H}_2\text{S}}$ values (as low as
458 -14.2‰) in several deposits (e.g., the Zhengguang gold deposit; [Fu et al. 2014](#)),
459 whereas the dominance of the Derbugan fault area by igneous rocks ensured that
460 deposits in this area had $\delta^{34}\text{S}_{\text{H}_2\text{S}}$ values close to zero.

461 **Lead sources.** In order to identify the source of lead and, by extension, the other
462 metals, we have compared the lead isotope compositions of the Chalukou sulfides
463 with those for sulfides from numerous ore deposits in the region, the Mesozoic granite,
464 basalt and trachyte, and the Duobaoshan Formation andesitic tuff ([Fig. 12](#)). In general,
465 the in situ lead isotope data are similar to those of previous studies of sulfides using
466 mineral separates at Chalukou and other Mesozoic ore deposits in the region
467 ([Appendix Table A2](#); [Guo et al. 2010](#); [Chu et al. 2012](#); [Zhao et al. 2016](#)), all of which
468 plot in a field between the mantle and orogen evolutionary curves ([Fig. 12](#); [Zartman](#)
469 [and Doe 1981](#)). The Paleozoic deposits, however, tend to have lower $^{208}\text{Pb}/^{204}\text{Pb}$ and
470 $^{207}\text{Pb}/^{204}\text{Pb}$ ratios at a given value of $^{206}\text{Pb}/^{204}\text{Pb}$, whereas those for the Mesozoic
471 deposits completely overlap the Chalukou data (e.g., [Liu et al. 2015b](#)), suggesting that
472 the Chalukou deposit and the other Mesozoic deposits had the same metal source ([Hu](#)
473 [et al. 2014](#); [Yuan et al. 2018](#)). Moreover, the Pb isotope data for the Chalukou ore
474 minerals are very similar to those for Mesozoic granites in the region ([Fig. 12](#)), further
475 indicating a Mesozoic magmatic source for the metals ([Hu et al. 2014](#); [Liu et al.](#)

476 [2014a](#), [2015a](#)). It is also important to note that, compared to the Chalukou sulfides,
477 the Pb isotopic data for the Mesozoic basalt and trachyte show distinctly higher
478 $^{206}\text{Pb}/^{204}\text{Pb}$ and $^{207}\text{Pb}/^{204}\text{Pb}$ ratios ([Fig. 12](#)), making these rocks less plausible
479 candidates for significant sources of metals for the Chalukou deposit.

480 **Metal signature of the fluid**

481 **Trace elements in pyrite.** Our results show that the trace element concentrations in
482 pyrite vary widely, underscoring the complexity of the ore-forming fluids ([Cook et al.](#)
483 [2013](#); [Mavrogenatos et al. 2020](#)). The Mo contents of Py-I (6.9 ± 3.8 ppm) and Py-II
484 (5 ± 128 ppm) are higher than those of Py-III (0.05 ± 5.7 ppm). The highest Mo
485 content was recorded by pyrite in Stage I and was high enough for the fluid to saturate
486 with molybdenite at high temperature (390-480°C; [Li et al. 2019](#)). The high solubility
487 of molybdenite at this temperature, however, ensured that its precipitation was limited,
488 thereby explaining the small proportion of molybdenite deposited during this stage.
489 Although the Cu content of pyrite was high in Stage I, the fluid did not saturate with a
490 Cu mineral (e.g., chalcopyrite). We attribute this to the fact that at the relatively high
491 temperature of Stage I, the solubility of copper minerals like chalcopyrite is too high
492 for them to saturate in the fluid ([Landtwing et al. 2005](#); [Williams-Jones and Migdisov](#)
493 [2014](#)). The Mo content of Py-II is slightly lower than that of Py-I, but was high
494 enough in the corresponding fluid for molybdenite to have been strongly
495 oversaturated and deposit the bulk of the molybdenite in Stage II ([Fig. 13](#)). This
496 reflects the fact that with decreasing temperature, the solubility of molybdenite
497 decreases sharply ([Williams-Jones and Migdisov 2014](#)). The low content of Cu in

498 pyrite of Stage II is consistent with the observation that the fluid did not saturate with
499 a Cu-bearing sulfide during this stage. The Mo/Cu ratio recorded by pyrite reached its
500 maximum in Stage II. By Stage III, however, the combination of a sharply higher Cu
501 content in the fluid and lower temperature allowed the fluid to saturate with
502 chalcopyrite. The extremely low Mo content in Py-III precluded precipitation of
503 molybdenite and the Mo/Cu ratio of the ore fluid reached its minimum (Fig. 9F).
504 From the observations discussed above, we conclude that pyrite recorded the chemical
505 evolution in the Mo/Cu ratio of the ore fluid, and that, in reaching its maximum
506 Mo/Cu ratio in Stage II, pyrite recorded the onset of main stage of molybdenite
507 deposition. We also conclude that the absolute content of metal in the fluid is not the
508 key factor affecting metal precipitation, but that ore mineral saturation controlled by
509 the system temperature is the real key.

510 **Trace elements in molybdenite.** Several studies have investigated the uptake of
511 trace elements by molybdenite and its use in predicting the trace element signature of
512 ore fluids (e.g., Ciobanu et al. 2013; Huang et al. 2014; Ren et al. 2018; McFall et al.
513 2019). Molybdenum is present in molybdenite as Mo^{4+} , which has a large ionic radius
514 that, together with its high charge, makes it difficult for trace metals such as Fe, Cu,
515 Zn, As, Pb, Co and Ni to substitute for it in concentrations of more than a few tens of
516 ppm (Ren et al. 2018). Because of the relatively high crystallization temperature of
517 molybdenite, the trace element composition of molybdenite could be, nevertheless,
518 important in recording the signature of the mineralizing fluid (Huang et al. 2014).

519 The trace element contents of Mol-I and Mol-II in the Chalukou deposit are clearly

520 different. Whereas Mol-I contains up to several hundred ppm of Ti, Mn, Fe, Pb and
521 several tens of ppm of Cu, As, Se, Ag, Sn, and Bi (Fig. 6), Mol-II contains thousands
522 of ppm of Ti, Fe, and Pb, and concentrations of several other trace metals are in the
523 range of tens to hundreds of ppm (Fig. 6). The observation that Mol-II is more
524 enriched in trace metals than Mol-I is consistent with greater metal enrichment in the
525 ore fluid in Stage II compared to Stage I. Given that the bulk of the molybdenite was
526 deposited in Stage II, the high metal content of Mol-II is an important signature of the
527 mineralizing fluid at Chalukou and potentially at other deposits.

528 **The role of magma Mo content**

529 The mechanism of metal enrichment in giant porphyry deposits has been a
530 contentious issue because of the large amounts of metal required to form these
531 deposits (Audétat et al. 2000, 2008; Richards 2003, 2011; Heinrich 2005; Pettke et al.
532 2010; Hou et al. 2015; Chang et al. 2018). Such large amounts of metal could be
533 extracted from a very large volume of magma with a low metal content, or a smaller
534 volume of magma with a high metal content (Core et al. 2006; Yang et al. 2016).
535 Which of these possibilities reflects reality, however, is still debated (Carten et al.
536 1988; Stern et al. 2007; Audétat 2010). In the case of Cu, the presence of
537 anhydrite-bearing intrusive rocks in the El Teniente Cu-Mo deposit containing >0.5%
538 Cu supports the argument that the source magma was unusually enriched in this metal
539 (Stern et al. 2007). Thus, the availability of a fertile magma (metal enriched) could be
540 an essential step in forming porphyry deposits (Nadeau et al. 2010; Chiaradia 2013).
541 In the case of Mo, which is a highly incompatible element and, thus, is preferentially

542 concentrated in the continental crust, a contribution of metal from this source could
543 lead to a fertile magma and thereby help explain the formation of giant porphyry Mo
544 deposits.

545 Audétat (2010), noting that the Mo content in the initial magma recorded by melt
546 inclusion data is relatively low (5-6 ppm), has argued that the magmas and fluids in
547 mineralized Mo systems are not unusually Mo-rich. Thus, in this model, a large
548 amount of magma would be needed to form a large porphyry Mo deposit. Similar
549 conclusions have been reached by Wang et al. (2014) and Zhang and Audétat (2017).
550 The processes by which metals form giant ore deposits from magmas containing a
551 very low Mo content, however, are still unclear.

552 In principle, the magmas forming the pre-ore monzogranite or those forming the
553 syn-ore intrusions could have been the source of Mo for the Chalukou deposit. The
554 two analyzed samples of monzogranite have Mo contents of 0.2 ppm, which is lower
555 than that of the average upper continental crust (0.8 ppm, Rudnick and Gao 2014). In
556 contrast, the unaltered syn-ore granite porphyry, quartz porphyry and fine-grained
557 porphyry contain 1-68 ppm (median, 18 ppm), 5-110 ppm (median, 9 ppm) and 3-96
558 ppm (median, 25 ppm) Mo, respectively (Li et al. 2014). This enrichment of the
559 syn-ore granites in Mo by a factor of 45 to 125 relative to the pre-ore monzogranite
560 and the extremely low Mo content of the latter makes it extremely unlikely that the
561 pre-ore monzogranite magmas were the source of the Mo for the Chalukou deposit
562 (Fig. 13). Thus, although the Mo content of the magmas forming some giant Mo
563 deposits may have been relatively low (Audétat 2010; Zhang and Audétat 2017), our

564 data leave little doubt that the Mo-rich syn-ore magmas at Chalukou were the source
565 of the Mo for this deposit.

566 A feature of the whole-rock geochemical data is the very low Sr/Y ratio (Sr/Y from
567 0.4 to 37; mean, 7) of the Mo-enriched syn-ore intrusions compared to the pre-ore
568 monzogranite (Sr/Y from 14 to 69; mean, 37) (Li et al. 2014; Liu et al. 2015a). This
569 could indicate that the magmas forming the syn-ore intrusions were derived from the
570 magma after an unusually high degree of fractional crystallization of plagioclase.
571 Such fractional crystallization would have greatly reduced the Sr content of the
572 residual magma (Kobylinski et al. 2020), thereby explaining the very low Sr/Y ratios
573 of the syn-ore intrusions. In turn, this could also explain the extremely strong negative
574 Eu anomalies of the syn-ore intrusions. Indeed, according to Li et al. (2014),
575 fractional crystallization of the main rock-forming minerals could have reached up to
576 50%, which could have significantly enriched the residual magma in Mo. However,
577 even considering the very high melt/silicate mineral partition coefficients reported for
578 Mo (35-1080 at 2.61 GPa and 600-800 °C; Bali et al. 2012), the Mo enrichment due
579 to fractional crystallization would only have increased the concentration of Mo in the
580 magma to 0.4 ppm.

581 Although the pre-ore monzogranite and syn-ore intrusions at Chalukou have similar
582 Sr-Nd-Hf isotope compositions, which permit them being genetically related (Liu et al.
583 2015a), the negative initial Hf isotope signature (ϵ_{Hf}) of the syn-ore intrusions (-1.4
584 to +0.5) indicates that their magmas assimilated old continental crust, which was not
585 the case for the pre-ore barren monzogranite (+0.9 to +3.0). As Mo is a highly

586 incompatible element and, therefore, concentrates in the crust, assimilation of old
587 continental crust likely explains the high Mo concentration of Mo in the syn-ore
588 intrusions ([Zhang and Li 2017](#)).

589 **IMPLICATIONS**

590 The trace element chemistry of pyrite and S and Pb isotopic compositions have
591 made it possible to interpret the evolution of hydrothermal fluids during the formation
592 of the Chalukou porphyry Mo deposit. This evolution occurred in three paragenetic
593 stages characterized by distinctive mineral assemblages. The composition of the fluid
594 as recorded by pyrite indicates that the fluids in Stage I and Stage II were enriched in
595 Mo, whereas the fluid in Stage III was highly depleted in Mo. The combination of a
596 relatively high Mo content of the fluid in Stage II (compared to the fluid in Stage III)
597 and lower temperature (compared to Stage I), caused the fluid to be highly
598 oversaturated with respect to molybdenite, and explains why molybdenite was
599 deposited mainly in Stage II. This leads to the conclusion that the absolute content of
600 metal in the ore fluid was not the key factor controlling metallic mineral deposition,
601 and that molybdenite saturation was controlled by the system temperature. Another
602 important conclusion of the study is that magmas that were unusually enriched in Mo
603 due to crustal contamination, and crystallized the syn-ore intrusions, were the most
604 plausible source of Mo for the Chalukou deposit. This shows, contrary to previous
605 studies, that magma fertility (enrichment in Mo) may play an essential role in
606 generating large porphyry Mo deposits. Finally, the study highlights the importance of
607 in situ compositional analyses (including S and Pb isotopes and trace elements) of ore

608 sulfides as tools for constraining the origin and chemical evolution of ore fluids that
609 should find widespread application well beyond porphyry Mo ore genesis.

610 **ACKNOWLEDGMENTS AND FUNDING**

611 This research was supported financially by the National Natural Science
612 Foundation of China (42122012, 41503042), the Fundamental Research Funds for the
613 Central Universities (QZ05201904), and the 111 Project of the Ministry of Science
614 and Technology (BP0719021). We thank Li Su and Hongyu Zhang (CUGB) for
615 performing sulfide in situ trace element analyses. DZ was supported financially by the
616 China Scholarship Council (CSC) (201906405012) to visit McGill University.
617 Constructive suggestions from Constantinos Mavrogenatos and an anonymous
618 reviewer, Associate Editor Paul Tomascak and Editor-in-Chief Hongwu Xu
619 significantly improved this manuscript.

620 **REFERENCES CITED**

- 621 Audétat, A., Gunther, D., and Heinrich, C.A. (2000) Causes for large-scale metal
622 zonation around mineralized plutons: Fluid inclusion LA-ICP-MS evidence from
623 the Mole Granite, Australia. *Economic Geology*, 95, 1563–1581.
- 624 Audétat, A., Pettke, T., Heinrich, C.A., and Bodnar, R.J. (2008) The composition of
625 magmatic-hydrothermal fluids in barren and mineralized intrusions. *Economic*
626 *Geology*, 103, 877–908.
- 627 Audétat, A. (2010) Source and evolution of molybdenum in the porphyry-Mo(-Nb)
628 deposit at Cave Peak, Texas. *Journal of Petrology*, 51, 1739–1760.

- 629 Bali, E., Keppler, H., and Audétat, A. (2012) The mobility of W and Mo in subduction
630 zone fluids and the Mo-W-Th-U systematics of island arc magmas. *Earth and*
631 *Planetary Science Letters*, 351–352, 195–207.
- 632 Blevin, P.L. (2002) The petrographic and compositional character of variably
633 K-enriched magmatic suites associated with Ordovician porphyry Cu-Au
634 mineralisation in the Lachlan Fold Belt, Australia. *Mineralium Deposita*, 37, 87–
635 99.
- 636 Camus, F. (1975) Geology of the El Teniente orebody with emphasis on wallrock
637 alteration. *Economic Geology*, 70, 1341–1372.
- 638 Carten, R.B., Geraghty, E.P., Walker, B.M., and Shannon, J.R. (1988) Cyclic
639 development of igneous features and their relationship to high-temperature
640 hydrothermal features in the Henderson porphyry molybdenum deposit,
641 Colorado. *Economic Geology*, 83, 266–296.
- 642 Carten, R.B., White, W.H., and Stern, H. (1993) High-grade granite-related
643 molybdenum systems: Classification and origin. *Geological Association of*
644 *Canada - Special Paper*, 40, 521–554.
- 645 Chang, J., Li, J.W., and Audétat, A. (2018) Formation and evolution of multistage
646 magmatic-hydrothermal fluids at the Yulong porphyry Cu-Mo deposit, Eastern
647 Tibet: Insights from LA-ICP-MS analysis of fluid inclusions. *Geochimica et*
648 *Cosmochimica Acta*, 232, 181–205.
- 649 Chen, Z.G., Zhang, L.C., Wan, B., Wu, H.Y., and Cleven, N. (2011) Geochronology
650 and geochemistry of the Wunugetushan porphyry Cu-Mo deposit in NE China,

- 651 and their geological significance. *Ore Geology Reviews*, 43, 92–105.
- 652 Chen, Y.J., Zhang, C., Li, N., Yang, Y.F., and Deng, K. (2012) Geology of the Mo
653 deposits in northeast China. *Journal of Jilin University (Earth Science Edition)*,
654 42, 1224–1268 (in Chinese with English abstract).
- 655 Chen, Y.J., Zhang, C., Wang, P., Pirajno, F., and Li, N. (2017) The Mo deposits of
656 northeast China: A powerful indicator of tectonic settings and associated
657 evolutionary trends. *Ore Geology Reviews*, 81, 602–640.
- 658 Chiaradia, M. (2013) Copper enrichment in arc magmas controlled by overriding
659 plate thickness. *Nature Geoscience*, 7, 43–46.
- 660 Chu, S.X., Liu, J.M., Xu, J.H., Wei, H., Chai, H., and Tong, K.Y. (2012) Zircon U-Pb
661 dating, petrogenesis and tectonic significance of the granodiorite in the
662 Sankuanggou skarn Fe-Cu deposit, Heilongjiang Province. *Acta Petrologica
663 Sinica*, 28, 433–450 (in Chinese with English abstract).
- 664 Ciobanu, C.L., Cook, N.J., Kelson, C.R., Guerin, R., Kalleske, N., and Danyushevsky,
665 L. (2013) Trace element heterogeneity in molybdenite fingerprints stages of
666 mineralization. *Chemical Geology*, 347, 175–189.
- 667 Clark, A.H., Farrar, E., Kontak, D.J., Langridge, R.J., Arenas, M., France, L.J.,
668 McBride, S.L., Woodman, P.I., Wasteneys, H.A., Sandeman, H.A., and Archibald,
669 D.A. (1990) Geologic and geochronologic constraints on the metallogenic
670 evolution of the Andes of southeastern Peru. *Economic Geology*, 85, 1520–1583.
- 671 Cook, N.J., Ciobanu, C.L., Meria, D., Silcock, D., and Wade, B. (2013)
672 Arsenopyrite-pyrite association in an orogenic gold ore: Tracing mineralization

- 673 history from textures and trace elements. *Economic Geology*, 108, 1273–1283.
- 674 Core, D.P., Kesler, S.E., and Essene, E.J. (2006) Unusually Cu-rich magmas
675 associated with giant porphyry copper deposits: Evidence from Bingham, Utah.
676 *Geology*, 34, 41–44.
- 677 Deng, K., Liu, Q.G., Chen, Y.J., Zhang, C., Zhu, X.F., and Xu, Q.W. (2018)
678 Geochronology geochemistry and Sr-Nd-Pb-Hf isotopes of the Early Jurassic
679 granodiorite from the Sankuanggou intrusion, Heilongjiang Province,
680 Northeastern China: Petrogenesis and geodynamic implications. *Lithos*, 296–299,
681 113–128.
- 682 Duan, P.X., Liu, C., Mo, X.X., Deng, D.F., Qin, J.H., Zhang, Y., and Tian, S.P. (2018)
683 Discriminating characters of ore-forming intrusions in the super-large Chalukou
684 porphyry Mo deposit, NE China. *Geoscience Frontiers*, 9, 1417–1431.
- 685 Fritzell, E.H., Bull, A.L., and Shephard, G.E. (2016) Closure of the Mongol–Okhotsk
686 Ocean: Insights from seismic tomography and numerical modelling. *Earth and
687 Planetary Science Letters*, 445, 1–12.
- 688 Fu, J.J., Zhao, Y.Y., Zeng, H., and Li, Y. (2014) Chronological and isotopic
689 characteristics of Zhengguang gold deposit in Heilongjiang Province, China.
690 *Acta Geologica Sinica-English Edition*, 88, 718–719.
- 691 Gao, B.Y., Zhang, L.C., Jin, X.D., Li, W.J., Chen, Z.G., and Zhu, M.T. (2016)
692 Geochronology and geochemistry of the Badaguan porphyry Cu-Mo deposit in
693 Derbugan metallogenic belt of the NE China, and their geological significances.
694 *International Journal of Earth Sciences*, 105, 507–519.

- 695 Gao, Y.Z., Xue, C.J., Lv, X.B., Zhao, X.B., Yang, Y.S., and Li, C.C. (2017) Genesis of
696 the Zhengguang gold deposit in the Duobaoshan ore field, Heilongjiang Province,
697 NE China: Constraints from geology, geochronology and S-Pb isotopic
698 compositions. *Ore Geology Reviews*, 84, 202–217.
- 699 Ge, W.C., Chen, J.S., Yang, H., Zhao, G.C., Zhang, Y.L., and Tian, D.X. (2015)
700 Tectonic implications of new zircon U-Pb ages for the Xinghuadukou Complex,
701 Erguna Massif, northern Great Xing'an Range, NE China. *Journal of Asian Earth
702 Sciences*, 106, 169–185.
- 703 Guo, F., Fan, W.M., Gao, X.F., Li, C.W., Miao, L.C., Zhao, L., and Li, H.X. (2010)
704 Sr-Nd-Pb isotope mapping of Mesozoic igneous rocks in NE China: Constraints
705 on tectonic framework and Phanerozoic crustal growth. *Lithos*, 120, 563–578.
- 706 Heinrich, C.A. (2005) The physical and chemical evolution of low-salinity magmatic
707 fluids at the porphyry to epithermal transition: A thermodynamic study.
708 *Mineralium Deposita*, 39, 864–889.
- 709 Hou, Z.Q., Yang, Z.M., Lu, Y.J., Kemp, A., Zheng, Y.C., Li, Q.Y., Tang, J.X., Yang,
710 Z.S., and Duan, L.F. (2015) A genetic linkage between subduction- and
711 collision-related porphyry Cu deposits in continental collision zones. *Geology*,
712 43, 247–250.
- 713 Hou, Z.S. (2014) Ore genesis and tectonic setting of Badaguan copper-molybdenum
714 deposit in Erguna region, Inner Mongolia, 66 p. Master's thesis, Jilin University,
715 Changchun (in Chinese with English abstract).
- 716 Hu, X.L., Yao, S.Z., He, M.C., Ding, Z.J., Liu, M., Cui, Y.B., and Shen, J. (2014)

- 717 Sulfur and lead isotopic characteristics of Chalukou and Daheishan porphyry Mo
718 deposits in northern segment of Da Hinggan Mountains. *Mineral Deposits*, 33,
719 776–784 (in Chinese with English abstract).
- 720 Huang, F., Wang, D.H., Chen, Y.C., Wang, C.H., Tang, J.X., Chen, Z.H., Wang, L.Q.,
721 Liu, S.B., Li, J.K., Zhang, C.Q., Ying, L.J., Wang, Y.L., Li, L.X., and Li, C.
722 (2014) Trace elements characteristics of molybdenites from endogenous
723 molybdenum deposits in China. *Mineral Deposits*, 33, 1193–1212 (in Chinese
724 with English abstract).
- 725 Huang, Q.H., Cheng, H.G., Han, M.X., Jin, X.Y., and Zhou, W.J. (2018) Sulfur
726 isotope characteristics of the late Paleozoic strata in No. D101 well at western
727 Songliao Basin. Joint meetings on the 12th National Congress of the
728 Palaeontological Society of China (PSC) and the 29th Annual Conference of PSC,
729 S11–04 (in Chinese).
- 730 Jin, L.Y., Qin, K.Z., Meng, Z.J., Li, G.M., Song, G.X., Li, Z.Z., Lv, K.P., Kan, X.S.,
731 and Zhao, C. (2014) Vein features and occurrences in Chalukou giant
732 molybdenum-zinc-lead deposit, northern Great Xing'an Range, and its
733 indications for mineralization. *Mineral Deposits*, 33, 742–760 (in Chinese with
734 English abstract).
- 735 Johnson, M.F., Wang, C.Y., and Wang, P. (2001) Continental island from the Upper
736 Silurian (Ludfordian Stage) of Inner Mongolia: Implications for eustasy and
737 paleogeography. *Geology*, 29, 955–958.
- 738 Kang, Y.J. (2015) The Ore-forming processes and mineralization of Badaguan

- 739 porphyry Cu-Mo deposit, Inner Mongolia, 112 p. Master's thesis, Chinese
740 Academy of Geological Sciences, Beijing (in Chinese with English abstract).
- 741 Kobylinski, C., Hattori, K., Smith, S., and Plouffe, A. (2020) Protracted magmatism
742 and mineralized hydrothermal activity at the Gibraltar porphyry
743 copper-molybdenum deposit, British Columbia. *Economic Geology*, 115, 1119–
744 1136.
- 745 Landtwing, M.R., Pettke, T., Halter, W.E., Heinrich, C.A., Redmond, P.B., Einaudi,
746 M.T., and Kunze, K. (2005) Copper deposition during quartz dissolution by
747 cooling magmatic-hydrothermal fluids: The Bingham porphyry. *Earth and*
748 *Planetary Science Letters*, 235, 229–243.
- 749 Lee, C-T.A., Luffi, P., Chin, E.J., Bouchet, R., Dasgupta, R., and Morton, D.M. (2012)
750 Copper systematics in arc magmas and implications for crust-mantle
751 differentiation. *Science*, 336, 64–68.
- 752 Lee, C-T.A., and Tang, M. (2020) How to make porphyry copper deposits. *Earth and*
753 *Planetary Science Letters*, 529, 115868.
- 754 Li, Z.Z., Qin, K.Z., Li, G.M., Ishihara, S., Jin, L.Y., Song, G.X., and Meng, Z.J. (2014)
755 Formation of the giant Chalukou porphyry Mo deposit in northern Great Xing'an
756 Range, NE China: Partial melting of the juvenile lower crust in intra-plate
757 extensional environment. *Lithos*, 202, 138–156.
- 758 Li, Z.Z., Qin, K.Z., Li, G.M., Jin, L.Y., and Song, G.X. (2018) Neoproterozoic and
759 early Paleozoic magmatic records from the Chalukou ore district, northern Great
760 Xing'an Range, NE China: Implications for tectonic evolution and Mesozoic Mo

- 761 mineralization. *Journal of Asian Earth Sciences*, 165, 96–113.
- 762 Li, Z.Z., Qin, K.Z., Li, G.M., Jin, L.Y., and Song, G.X. (2019) Incursion of meteoric
763 water triggers molybdenite precipitation in porphyry Mo deposits: A case study
764 of the Chalukou giant Mo deposit. *Ore Geology Reviews*, 109, 144–162.
- 765 Liu, J., Mao, J.W., Wu, G., Wang, F., Luo, D.F., Hu, Y.Q., and Li, T.G. (2014a) Fluid
766 inclusions and H-O-S-Pb isotope systematics of the Chalukou giant porphyry Mo
767 deposit, Heilongjiang Province, China. *Ore Geology Reviews*, 59, 83–96.
- 768 Liu, J., Mao, J.W., Wu, G., Wang, F., Luo, D.F., and Hu, Y.Q. (2014b) Zircon U-Pb
769 and molybdenite Re-Os dating of the Chalukou porphyry Mo deposit in the
770 northern Great Xing'an Range, China and its geological significance. *Journal of*
771 *Asian Earth Sciences*, 79, 696–709.
- 772 ——— (2015a) Geochemical signature of the granitoids in the Chalukou giant
773 porphyry Mo deposit in the Heilongjiang Province, NE China. *Ore Geology*
774 *Reviews*, 64, 35–52.
- 775 Liu, J., Zhou, Z.H., He, Z.F., and Ouyang, H.G. (2015b) Zircon U-Pb dating and
776 geochemistry of ore-bearing tonalite in Tongshan copper deposit, Heilongjiang
777 Province. *Mineral Deposits*, 34, 289–308 (in Chinese with English abstract).
- 778 Liu, Y.F., Bagas, L., Jiang, S.H., and Wang, F.X. (2017) The Chalukou deposit in the
779 North Great Xing'an Range of China: A protracted porphyry Mo ore-forming
780 system in a long-lived magmatic evolution cycle. *Ore Geology Reviews*, 89,
781 171–186.
- 782 Ma, D.Y. (1984) Isotope geology of the Duobaoshan copper ore field. *Mineral*

- 783 Deposits, 3, 47–57 (in Chinese with English abstract).
- 784 Mao, J.W., Pirajno, F., Xiang, J.F., Gao, J.J., Ye, H.S., Li, Y.F., and Guo, B.J. (2011)
785 Mesozoic molybdenum deposits in the east Qinling-Dabie orogenic belt:
786 Characteristics and tectonic settings. *Ore Geology Reviews*, 43, 264–293.
- 787 Mathur, R., Ruiz, J., Titley, S., Gibbins, S., and Margotomo, W. (2000) Different
788 crustal sources for Au-rich and Au-poor ores of the Grasberg Cu-Au porphyry
789 deposit. *Earth and Planetary Science Letters*, 183, 7–14.
- 790 Mavrogonatos, C., Voudouris, P., Zaccarini, F., Klemme, S., Berndt, J., Tarantola, A.,
791 Melfos, V., and Spry, P.G. (2020) Multi-stage introduction of precious and
792 critical metals in pyrite: A case study from the Konos Hill and Pagoni Rachi
793 porphyry/epithermal prospects, NE Greece. *Minerals*, 10, 784.
- 794 McFall, K., Roberts, S., McDonald, I., Boyce, A.J., Naden, J., and Teagle, D. (2019)
795 Rhenium enrichment in the Muratdere Cu-Mo (Au-Re) porphyry deposit, Turkey:
796 Evidence from stable isotope analyses ($\delta^{34}\text{S}$, $\delta^{18}\text{O}$, δD) and laser
797 ablation-inductively coupled plasma-mass spectrometry analysis of sulfides.
798 *Economic Geology*, 114, 1443–1466.
- 799 Mi, K.F., Liu, Z.J., Li, C.F., Liu, R.B., Wang, J.P., and Peng, R.M. (2017) Origin of
800 the Badaguan porphyry Cu-Mo deposit, Inner Mongolia, Northeast China:
801 Constraints from geology isotope geochemistry and geochronology. *Ore Geology*
802 *Reviews*, 81, 154–172.
- 803 Nadeau, O., Williams-Jones, A.E., and Stix, J. (2010) Sulphide magma as a source of
804 metals in arc-related magmatic hydrothermal ore fluids. *Nature Geoscience*, 3,

- 805 501–505.
- 806 Nie, F.J., Sun, Z.J., Li, C., Liu, Y.F., Lv, K.P., Zhang, K., and Liu, Y. (2011) Re-Os
807 isotopic dating of molybdenite separates from Chalukou porphyry Mo
808 polymetallic deposit in Heilongjiang Province. *Mineral Deposits*, 30, 828–836
809 (in Chinese with English abstract).
- 810 Olson, N.H., Dilles, J.H., Kent, A.J.R., and Lang, J.R. (2017) Geochemistry of the
811 Cretaceous Kaskanak Batholith and genesis of the Pebble porphyry Cu-Au-Mo
812 deposit, Southwest Alaska. *American Mineralogist*, 102, 1597–1621.
- 813 Pettke, T., Oberli, F., and Heinrich, C.A. (2010) The magma and metal source of giant
814 porphyry-type ore deposits based on lead isotope microanalysis of individual
815 fluid inclusions. *Earth and Planetary Science Letters*, 296, 267–277.
- 816 Ren, Z., Zhou, T.F., Hollings, P., White, N.C., Wang, F.Y., and Yuan, F. (2018) Trace
817 element geochemistry of molybdenite from the Shapinggou super-large porphyry
818 Mo deposit, China. *Ore Geology Reviews*, 95, 1049–1065.
- 819 Richards, J.P. (2003) Tectono-magmatic precursors for porphyry Cu- (Mo) deposit
820 formation. *Economic Geology*, 98, 1515–1531.
- 821 ——— (2011) High Sr/Y arc magmas and porphyry Cu ± Mo ± Au deposits: Just add
822 water. *Economic Geology*, 106, 1075–1081.
- 823 Rudnick, R.L., and Gao, S. (2014) Composition of the continental crust. In R.L.
824 Rudnick, Eds., *Treatise on geochemistry*, 1–51. Elsevier, Amsterdam.
- 825 Seal, R.R. (2006) Sulfur isotope geochemistry of sulfide minerals. *Reviews in*
826 *Mineralogy and Geochemistry*, 61, 633–677.

- 827 Shi, P.H., Yang, Y.C., Ye, S.Q., and Han, S.J. (2012) Geological and geochemical
828 characteristics and genesis of ferromolybdenum deposit in Wudaoling,
829 Heilongjiang Province. *Global Geology*, 31, 262–270 (in Chinese with English
830 abstract).
- 831 Shu, Q.H., Chang, Z.S., Lai, Y., Zhou, Y.T., Sun, Y., and Yan, C. (2016) Regional
832 metallogeny of Mo-bearing deposits in northeastern China with new Re-Os dates
833 of porphyry Mo deposits in the northern Xilamulun district. *Economic Geology*,
834 111, 1783–1798.
- 835 Shu, Q.H., and Chiaradia, M. (2021) Mesozoic Mo mineralization in northeastern
836 China did not require regional-scale pre-enrichment. *Economic Geology*, 116,
837 1227–1237.
- 838 Sillitoe, R.H. (2010) Porphyry copper systems. *Economic Geology*, 105, 3–41.
- 839 Stern, C.R., Funk, J.A., Skewes, M.A., and Alejandra, A. (2007) Magmatic anhydrite
840 in plutonic rocks at the El Teniente Cu-Mo deposit, Chile, and the role of sulfur-
841 and copper-rich magmas in its formation. *Economic Geology*, 102, 1335–1344.
- 842 Tang, W.L., Zeng, W., Ran, H., Zhou, Y., and Sun, W.L. (2012) Geological features
843 and ore prospecting of Biligangan deposit, Abaga, Inner Mongolia. *Geological*
844 *Survey and Research*, 35, 161–166 (in Chinese with English abstract).
- 845 Todt, W., Cliff, R.A., Hanser, A., and Hofmann, A.W. (1993) Recalibration of NBS
846 lead standards using a $^{207}\text{Pb}/^{205}\text{Pb}$ double spike. *Terra Abstracts*, 5, 396.
- 847 Wang, G.G., Ni, P., Yu, W., Chen, H., Jiang, L.L., Wang, B.H., Zhang, H.D., and Li,
848 P.F. (2014) Petrogenesis of Early Cretaceous post-collisional granitoids at

- 849 Shapinggou, Dabie Orogen: Implications for crustal architecture and porphyry
850 Mo mineralization. *Lithos*, 184–187, 393–415.
- 851 Wang, G.R., Wu, G., Xu, L.Q., Li, X.Z., Liu, J., Zhang, T., Quan, Z.X., Wu, H., Li,
852 T.G., and Chen, Y.C. (2017) Molybdenite Re-Os age, H-O-C-S-Pb isotopes and
853 fluid inclusion study of the Caosiyao porphyry Mo deposit in Inner Mongolia,
854 China. *Ore Geology Reviews*, 81, 728–744.
- 855 Williams-Jones, A.E., and Migdisov, A.A. (2014) Experimental constraints on the
856 transport and deposition of metals in ore-forming hydrothermal systems. *Society*
857 *of Economic Geologists, Special Publication*, 18, 77–95.
- 858 Wu, F.Y., Sun, D.Y., Ge, W.C., Zhang, Y.B., Grant, M.L., Wilde, S.A., and Jahn, B.M.
859 (2011) Geochronology of the Phanerozoic granitoids in northeastern China.
860 *Journal of Asian Earth Sciences*, 41, 1–30.
- 861 Wu, G., Chen, Y.C., Sun, F.Y., Liu, J., Wang, G.R., and Xu, B. (2015) Geochronology
862 geochemistry and Sr-Nd-Hf isotopes of the early Paleozoic igneous rocks in the
863 Duobaoshan area, NE China, and their geological significance. *Journal of Asian*
864 *Earth Sciences*, 97, 229–250.
- 865 Xing, K., Shu, Q., Lentz, D.R., and Wang, F.Y. (2020) Zircon and apatite geochemical
866 constraints on the formation of the Huojihe porphyry Mo deposit in the Lesser
867 Xing'an Range, NE China. *American Mineralogist*, 105, 382–396.
- 868 Xiong, S.F., He, M.C., Yao, S.Z., Cui, Y.B., Shi, G.Z., Ding, Z.J., and Hu, X.L. (2015)
869 Fluid evolution of the Chalukou giant Mo deposit in the northern Great Xing'an
870 Range, NE China. *Geological Journal*, 50, 720–738.

- 871 Xu, B., Hou, Z.Q., Griffin, W.L., Lu, Y.J., Belousova, E., Xu, J.F., and O'Reilly S.Y.
872 (2021) Recycled volatiles determine fertility of porphyry deposits in collisional
873 settings. *American Mineralogist*, 106, 656–661.
- 874 Yang, L.Q., Deng, J., Gao, X., He, W.Y., Meng, J.Y., Santosh, M., Yu, H.J., Yang, Z.,
875 and Wang, D. (2016) Timing of formation and origin of the Tongchanggou
876 porphyry-skarn deposit: Implications for late Cretaceous Mo-Cu metallogenesis
877 in the southern Yidun Terrane, SE Tibetan Plateau. *Ore Geology Reviews*, 81,
878 1015–1032.
- 879 Yang, Z.M., Lu, Y.J., Hou, Z.Q., and Chang, Z.S. (2015) High-Mg diorite from
880 Qulong in southern Tibet: Implications for the genesis of adakite-like intrusions
881 and associated porphyry Cu deposits in collisional orogens. *Journal of Petrology*,
882 56, 227–254.
- 883 Yang, Z.M., and Cooke, D.R. (2019) Porphyry copper deposits in China. *Society of*
884 *Economic Geologists, Special Publication*, 22, 133–187.
- 885 Yuan, H., Liu, X., Chen, L., Bao, Z., Chen, K., and Zong, C. (2017) Simultaneous
886 measurement of sulfur and lead isotopes in sulfides using nanosecond laser
887 ablation coupled with two multi-collector inductively coupled plasma mass
888 spectrometers. *Journal of Asian Earth Sciences*, 154, 386–396.
- 889 Yuan, M.W., Li, S.R., Li, C.L., Santosh, M., Alam, M., and Zeng, Y.J. (2018)
890 Geochemical and isotopic composition of auriferous pyrite from the Yongxin
891 gold deposit, Central Asian Orogenic Belt: Implication for ore genesis. *Ore*
892 *Geology Reviews*, 93, 255–267.

- 893 Zartman, R.E., and Doe, B.R. (1981) Plumbotectonics. *The model Tectonophysics*, 75,
894 135–162.
- 895 Zeng, Q.D., Liu, J.M., Qin, K.Z., Fan, H.R., Chu, S.X., Wang, Y.B., and Zhou, L.L.
896 (2013) Types characteristics and time-space distribution of molybdenum deposits
897 in China. *International Geology Review*, 55, 1311–1358.
- 898 Zhai, D.G., Liu, J.J., Zhang, H.Y., Yao, M.J., Wang, J.P., and Yang, Y.Q. (2014) S-Pb
899 isotopic geochemistry, U-Pb and Re-Os geochronology of the Huanggangliang
900 Fe-Sn deposit, Inner Mongolia, NE China. *Ore Geology Reviews*, 59, 109–122.
- 901 Zhai, D.G., Liu, J.J., Zhang, A.L., and Sun, Y.Q. (2017) U-Pb, Re-Os and $^{40}\text{Ar}/^{39}\text{Ar}$
902 geochronology of porphyry Sn ± Cu ± Mo and polymetallic (Ag-Pb-Zn-Cu) vein
903 mineralization at Bianjiadayuan, Inner Mongolia, NE China: Implications for
904 discrete mineralization events. *Economic Geology*, 112, 2041–2059.
- 905 Zhai, D.G., Liu, J.J., Cook, N.J., Wang, X.L., Yang, Y.Q., Zhang, A.L., and Jiao, Y.C.
906 (2019) Mineralogical, textural, sulfur and lead isotope constraints on the origin
907 of Ag-Pb-Zn mineralization at Bianjiadayuan, Inner Mongolia, NE China.
908 *Mineralium Deposita*, 54, 47–66.
- 909 Zhai, D.G., Williams-Jones, A.E., Liu, J.J., Selby, D., Voudouris, P.C., Tombros, S., Li,
910 K., Li, P.L., and Sun, H.J. (2020) The genesis of the giant Shuangjianzishan
911 epithermal Ag-Pb-Zn deposit, Inner Mongolia, Northeastern China. *Economic*
912 *Geology*, 115, 101–128.
- 913 Zhang, F.F., Wang, Y.H., Liu, J.J., Wang, J.P., Zhao, C.B., and Song, Z.W. (2016)
914 Origin of the Wunugetushan porphyry Cu-Mo deposit, Inner Mongolia, NE

- 915 China: Constraints from geology, geochronology, geochemistry, and isotopic
916 compositions. *Journal of Asian Earth Sciences*, 117, 208–224.
- 917 Zhang, C., and Li, N. (2017) Geochronology and zircon Hf isotope geochemistry of
918 granites in the giant Chalukou Mo deposit, NE China: Implications for tectonic
919 setting. *Ore Geology Reviews*, 81, 780–793.
- 920 Zhang, D.H., and Audétat, A. (2017) Chemistry mineralogy and crystallization
921 conditions of porphyry Mo-forming magmas at Urad-Henderson and Silver
922 Creek, Colorado, USA. *Journal of Petrology*, 58, 277–296.
- 923 Zhang, Y.M., Gu, X.X., Liu, R.P., Sun, X., Li, X.L., and Zheng, L. (2017) Geology,
924 geochronology and geochemistry of the Gaogangshan Mo deposit: A newly
925 discovered Triassic collision-type Mo mineralization in the Lesser Xing'an
926 Range, NE China. *Ore Geology Reviews*, 81, 672–688.
- 927 Zhang, H.Y., Su, L., Yang, L.M., Wang, D.C., Hu, X.L., Song, Y.T., and Xiong, L.
928 (2019) Study on LA-ICP-MS determination of trace elements in sulfide minerals.
929 *Hans Journal of Chemical Engineering and Technology*, 9, 401–409 (in Chinese
930 with English abstract).
- 931 Zhao, Y., Lv, J.C., Chen, J., Zhang, P., Xu, J., and Bi, Z.W. (2016) Geological and
932 S-Pb geochemical characteristics of Xinzhangfang molybdenum deposit in the
933 northern Greater Khingan Mountains region. *Nonferrous Metals*, 68, 18–23 (in
934 Chinese with English abstract).
- 935 Zhao, Q.Q., Zhai, D.G., Mathur, R., Liu, J.J., Selby, D., and Williams-Jones, A.E.
936 (2021a) The giant Chalukou porphyry Mo deposit, Northeast China: The product

937 of a short-lived, high flux mineralizing event. *Economic Geology*, 116, 1209–
938 1225.

939 Zhao, Q.Q., Zhai, D.G., Wang, J.P., Liu, J.J., and Williams-Jones, A.E. (2021b) The
940 geochemistry and geochronology of Permian granitoids from central Inner
941 Mongolia, NE China: Petrogenesis and tectonic implications. *Lithos*, 404–405,
942 106489.

943 Zheng, Y.F., Mao, J.W., Chen, Y.J., Sun, W.D., Ni, P., and Yang, X.Y. (2019)
944 Hydrothermal ore deposits in collisional orogens. *Science Bulletin*, 64, 67–74.

945 Zhou, J.B., Wilde, S.A., Zhang, X.Z., Zhao, G.C., Liu, F.L., Qiao, D.W., Ren, S.M.,
946 and Liu, J.H. (2011) A >1300 km late Pan-African metamorphic belt in NE
947 China: New evidence from the Xing'an block and its tectonic implications.
948 *Tectonophysics*, 509, 280–292.

949 Zhou, X., Fei, G.C., Zhou, Y., Wen, C.Q., Zhang, Y., and Yue, X.Y. (2015)
950 Chronology and crust-mantle mixing of ore-forming porphyry of the Bangongco:
951 Evidence from zircon U-Pb age and Hf isotopes of the Naruo porphyry
952 copper-gold deposit. *Acta Geologica Sinica-English Edition*, 89, 217–228.

953 Zorin, Y.A., Zorina, L., and Spiridonov, A.M. (2001) Geodynamic setting of gold
954 deposits in eastern and central Trans-Baikal (Chita Region Russia). *Ore Geology*
955 *Reviews*, 17, 215–232.

956

957 **Figure captions**

958 Fig. 1. (A) A schematic map of the Central Asian orogenic belt (CAOB; modified

959 from [Shu et al. 2016](#); [Zhai et al. 2019](#)); (B) A geological map of the northern Great
960 Hinggan Range showing the locations of major ore deposits (modified from [Chen et](#)
961 [al. 2017](#)).

962 Fig. 2. (A) A geological map of the Chalukou porphyry Mo deposit (modified from
963 [Xiong et al. 2015](#)); (B) A representative cross-section showing the local intrusions,
964 dikes and hydrothermal breccias (modified from [Li et al. 2014](#)); (C) A representative
965 cross-section showing the vertical distribution of different hydrothermal alteration
966 zones, and (D) A representative cross-section showing the vertical distribution of
967 Mo-bearing orebodies (modified from [Li et al. 2019](#)).

968 Fig. 3 Field and hand-specimen photographs of alteration in the Chalukou deposit. (A
969 and B) Field and hand-specimen photographs of silicic alteration; (C and D)
970 Molybdenite-quartz veins associated with potassic alteration; (E) Phyllic alteration
971 overprinting the earlier potassic alteration.

972 Fig. 4. (A) A photograph showing the stockwork ores; (B and C) The mode of
973 occurrence of molybdenite-pyrite-quartz-fluorite veins; (D) Martite after magnetite;
974 (E) Magnetite replaced by hematite; (F) Molybdenite (Mol-II) cross-cutting
975 early-formed pyrite (Py-I); (G) An early-formed pyrite (Py-I) vein; (H) Molybdenite
976 (Mol-II) cut by a pyrite (Py-II) vein; (I) Sphalerite intergrown with galena, pyrrhotite
977 and pyrite; (J) Pyrite (Py-III) associated with galena and sphalerite; (K) The
978 occurrence of molybdenite (Mol-III) in pyrite interstices.

979 Fig. 5. (A) A hand specimen showing two generations of molybdenite; (B)

980 Molybdenite (Mol-I) associated with pyrite (Py-I); (C) A molybdenite-quartz vein; (D)
981 An occurrence of molybdenite (Mol-II) as fine-grained aggregates; (E, F, G) An
982 occurrence of molybdenite (Mol-II) as wispy veinlets.

983 Fig. 6. Box and whisker plots showing the concentrations of trace elements in
984 different molybdenite generations analyzed by LA-ICP-MS.

985 Fig. 7. Binary plots of (A) Fe vs. Ti, (B) Fe vs. Cu, (C) Bi vs. Pb, (D) Bi vs. Ag, (E)
986 W vs. As and (F) Sb vs. Au for different molybdenite generations. Two samples show
987 anomalously high Ti contents (dashed ellipse), due probably to the presence of
988 mineral inclusions (e.g., ilmenite and rutile).

989 Fig. 8. Box and whisker plots showing the concentrations of trace elements in
990 different pyrite generations analyzed by LA-ICP-MS.

991 Fig. 9. Binary plots of (A) Pb vs. Ag, (B) Bi vs. Pb, (C) Mn vs. Zn, (D) Ti vs. Zn, (E)
992 Ni vs. Co and (F) Mo vs. Cu for different pyrite generations. See text for additional
993 explanation.

994 Fig. 10. Representative pyrite samples selected for in situ trace element analyses. (A)
995 Pyrite (Py-II) from stage II (A1 A hand specimen photo of Py-II bearing
996 mineralization; A2 A reflected light image of pyrite showing the spots of a
997 LA-ICP-MS analytical profile; A3 Time-resolved depth profiles of selected elements
998 for the spot shown in A2; A4 Concentrations of selected trace elements along the
999 profile shown in A2); (B) Pyrite (Py-III) from stage III (B1 A hand specimen
1000 photograph of Py-III bearing mineralization; B2 A reflected light image of pyrite

1001 showing the spots of a LA-ICP-MS analytical profile; B3 Time-resolved depth
1002 profiles of selected elements for the spot shown in B2; B4 Concentrations of selected
1003 trace elements along the profile shown in B2).

1004 Fig. 11. (A) A histogram of sulfur isotopic compositions ($\delta^{34}\text{S}_{\text{V-CDT}}$) for sulfides from
1005 the Chalukou porphyry Mo deposit; (B) A comparison of the sulfur isotopic
1006 compositions ($\delta^{34}\text{S}_{\text{H}_2\text{S}}$) of sulfide minerals from deposits in the Derbugan and
1007 Duobaoshan ore fields (data from [Ma 1984](#); [Chen et al. 2011](#); [Fu et al. 2014](#); [Hou](#)
1008 [2014](#); [Hu et al. 2014](#); [Kang 2015](#); [Liu et al. 2015b](#); [Zhang et al. 2016](#); [Zhao et al. 2016](#);
1009 [Gao et al. 2017](#); [Mi et al. 2017](#); [Yuan et al. 2018](#)).

1010 Fig. 12. Lead isotope compositions of sulfides from the Chalukou porphyry Mo
1011 deposit compared to local early Paleozoic volcano-sedimentary rocks, Mesozoic
1012 granite, basalt and trachyte, and local early Paleozoic to Mesozoic ore deposits (data
1013 from [Guo et al. 2010](#); [Chu et al. 2012](#); [Hu et al. 2014](#); [Liu et al. 2015b](#); [Zhao et al.](#)
1014 [2016](#); [Gao et al. 2017](#); [Mi et al. 2017](#); [Deng et al. 2018](#); [Yuan et al. 2018](#)). (A)
1015 $^{206}\text{Pb}/^{204}\text{Pb}$ vs. $^{208}\text{Pb}/^{204}\text{Pb}$ plots; (B) $^{206}\text{Pb}/^{204}\text{Pb}$ vs. $^{207}\text{Pb}/^{204}\text{Pb}$ plots. The arrows in
1016 the inset figures show that Moly-I, Moly-II and Py-II have more radiogenic Pb isotope
1017 compositions than those of the Stage III sulfides. The Pb isotope curves for the mantle,
1018 orogen, and crust were taken from [Zartman and Doe \(1981\)](#).

1019 Fig. 13. A summary plot showing bulk igneous rock Mo concentrations as well as Mo
1020 concentrations in different pyrite generations; The Mo contents of local intrusions are
1021 from [Li et al. \(2014\)](#) and [Liu et al. \(2015a\)](#) and the Mo contents of the sulfides are

1022 from this study. Spot with anomaly high element content (pink dotted line) is
1023 excluded.

1024

1025 Table 1. In situ trace element compositions of sulfides from the Chalukou porphyry
1026 Mo deposit

1027 Table 2. In situ sulfur isotopic compositions of sulfides from the Chalukou porphyry
1028 Mo deposit

1029 Table 3. In situ lead isotopic compositions of sulfides from the Chalukou porphyry
1030 Mo deposit

1031 Table 4. Whole rock lead isotopic compositions of intrusions from the Chalukou
1032 porphyry Mo deposit

1033

1034 Appendix Table 1A. S isotope data of sulfides from ore deposits in NE China

1035 Appendix Table 2A. Pb isotope data of sulfides from local ore deposits, Mesozoic
1036 granite, basalt, tracyte, and Duobaoshan Formation volcano-sedimentary rocks in NE
1037 China

1038

Table 1. In situ trace element compositions of sulfides from the Chalukou porphyry Mo deposit

Element (ppm)	Ti	V	Cr	Mn	Fe	Co	Ni	Cu	Zn	As	Se	Ag	Cd	Sn	Sb	W	Pb	Bi
<i>Mol-I (n=6)</i>																		
Max	152	31.8	88	296	4555	0.3	6.8	40.9	1250	6.6	70	22.5	54.9	20.6	3.2	207	424	106
Min	85	3.3	26.2	16	517	0.1	1.0	2.9	2.8	1.4	55	0.6	48.7	11.2	0.3	1.7	45	7
Mean	114	11.8	40.3	101	1570	0.2	3.8	18.1	217.1	3.4	63	8.4	51.5	13.3	1.3	53.8	261	55
Median	113	4.2	30.1	72	894	0.2	3.8	9.8	6.4	2.4	64	3.4	51.2	12	0.7	3	269	46
S.D.	28	12.8	23.8	109	1530	0.1	2.3	16.4	506.2	2.2	7	9.1	2.2	3.6	1.3	85.6	130	39
<i>Mol-II (n=7)</i>																		
Max	34247	103	308	560	11462	19	50	393	133	162	542	181	122	250	30.6	586	6041	1309
Min	187	6.2	37.5	67	1655	0.8	2.4	22.1	8.0	16.4	52	7.1	94.4	17.0	3.4	24.7	1239	159
Mean	5482	58.3	119.5	248	7298	4.4	11.3	153.1	37.3	105.2	143	90.1	104.1	70.4	21.7	321.5	4535	892
Median	312	59.9	74.9	233	7570	1.9	4.4	119	25.5	119.8	78	77.5	101.5	33.8	25.7	348.9	4519	910
S.D.	12718	29.6	97.3	152	3219	6.5	17.3	117.1	43.4	45.3	177	55.7	9.7	84.3	9.9	184.5	1622	373
Element (ppm)	Ti	V	Mn	Mo	Co	Ni	Cu	Zn	As	Se	Ag	Cd	Sn	Sb	W	Pb	Bi	U
<i>Py-I (n=5)</i>																		
Max	49.4	4.4	898	10627	19.2	744	118.7	3911	1845	11.5	15.2	22.8	22.8	8.4	10.1	344	74.2	5.7
Min	5.1	0.1	0.4	2.4	1.7	4	1.7	1	0.3	3.2	0.3	0.1	0.5	0.1	0.1	7	9.3	0.1
Mean	22.4	1.1	220.2	5.9	10.4	175	33.9	920	372	5.8	4.2	5.1	5.2	1.8	2.4	117	27.0	1.9
Median	13.8	0.3	75.3	6.9	12	19	8.7	26	1.6	5.0	2.3	0.2	0.9	0.1	0.5	24	15.5	0.9
S.D.	20.3	1.9	382.2	3.8	7.2	320.7	49.6	1696	823	3.2	6.2	9.9	9.9	3.7	4.3	151	27	2.4
<i>Py-II (n=12)</i>																		
Max	13.0	1.31	12.3	8075	87.8	63.7	7.3	5.7	8.0	35.3	1.68	1.5	1.3	0.45	6.47	65.2	13.9	0.81
Min	2.1	0.02	0.1	0.04	0.3	0.7	0.2	0.3	0.7	3.7	0.01	0.2	0.4	0.10	0.04	0.0	0.1	0.01
Mean	5.5	0.19	4.0	49.0	19.7	12.8	2.1	1.8	2.9	9.9	0.35	0.6	0.8	0.21	1.03	9.8	4.3	0.12
Median	3.1	0.06	3	5	10.1	5.3	1.3	1.4	1.4	7.3	0.11	0.3	0.5	0.15	0.2	4	1.3	0.03

S.D.	3.9	0.37	4.5	128.1	25.7	18.3	2.1	1.8	2.7	8.3	0.51	0.5	0.4	0.12	1.99	18.1	5.3	0.22
<i>Py-III (n=31)</i>																		
Max	5.5	0.09	7.75	31.19	43.5	277.8	2592	5.8	37	19.4	21	0.6	1.2	0.39	1.02	2243	44.2	0.21
Min	2.2	0.01	0.09	0.02	0.0	0.1	0.3	0.2	0.2	1.2	0.01	0.1	0.2	0.07	0.03	0.04	0.02	0.01
Mean	3.2	0.02	1.01	1.42	4.7	10.0	24.0	0.8	2.3	9.2	1.80	0.2	0.5	0.11	0.10	88.6	5.8	0.03
Median	3	0.02	0.14	0.05	0.1	0.6	8.7	0.4	0.5	8.1	0.05	0.2	0.4	0.1	0.06	0.17	0.3	0.02
S.D.	0.8	0.02	1.9	5.7	10.3	49.7	37.1	1.1	6.5	5.9	5.2	0.1	0.2	0.1	0.2	403.1	12	0.04

Note: S.D. = standard deviation values

Table 2 In situ sulfur isotopic compositions of sulfides from the Chalukou porphyry Mo deposit

No.	Sample No.	Depth (m)	Description	Mineral	$\delta^{34}\text{S}_{\text{V-CDT}}$ (‰)
1	16CLK-26-3-1	380	Py-FI and Qz-Py-Mol veins	Py-I	4.2
2	16CLK-26-3-2	380	Py-FI and Qz-Py-Mol veins	Py-I	3.2
3	16CLK-27-1--1	380	Mol-Py vein	Py-II	2.5
4	16CLK-27-2-1	380	Mol-Py vein	Py-II	2.1
5	16CLK-27-2-2	380	Mol-Py vein	Py-II	1.4
6	16CLK-27-2-3	380	Mol-Py vein	Py-II	2.4
7	16CLK-26-1-1	380	Py-FI and Qz-Py-Mol veins	Py-III	4.0
8	16CLK-26-1-2	380	Py-FI and Qz-Py-Mol veins	Py-III	2.9
9	16CLK-154-1-1	320	Py with minor Sp-Gn	Py-III	4.6
10	16CLK-154-1-2	320	Py with minor Sp-Gn	Py-III	3.9
11	16CLK-154-2-1	320	Py with minor Sp-Gn	Py-III	3.2
12	16CLK-154-3-1	320	Py with minor Sp-Gn	Py-III	2.0
13	16CLK-154-3-2	320	Py with minor Sp-Gn	Py-III	1.5
14	16CLK-154-3-3	320	Py with minor Sp-Gn	Py-III	1.1
15	16CLK-154-3-4	320	Py with minor Sp-Gn	Py-III	3.3
16	16CLK-154-3-5	320	Py with minor Sp-Gn	Py-III	3.0
17	16CLK-154-3-10	320	Py with minor Sp-Gn	Py-III	3.2
18	16CLK-26-2-1	380	Py-FI and Qz-Py-Mol veins	Mol-I	7.2
19	16CLK-26-3-1	380	Py-FI and Qz-Py-Mol veins	Mol-I	7.2
20	16CLK-154-1-3	320	Py with minor Sp-Gn	Mol-I	7.8
21	16CLK-27-1-1	380	Mol-Py vein	Mol-II	4.7
22	16CLK-27-1-2	380	Mol-Py vein	Mol-II	5.1
23	16CLK-27-2-4	380	Mol-Py vein	Mol-II	4.2
24	16CLK-27-2-5	380	Mol-Py vein	Mol-II	6.8
25	16CLK-154-2-2	320	Py with minor Sp-Gn	Sp	0.2
26	16CLK-154-2-3	320	Py with minor Sp-Gn	Sp	1.9
27	16CLK-154-3-8	320	Py with minor Sp-Gn	Sp	2.4
28	16CLK-154-3-9	320	Py with minor Sp-Gn	Sp	2.2
29	16CLK-154-3-6	320	Py with minor Sp-Gn	Gn	-5.0
30	16CLK-154-3-7	320	Py with minor Sp-Gn	Gn	-5.2

Abbreviations: FI = fluorite, Gn = galena, Mol = molybdenite, Py = pyrite, Qz = quartz, Sp = sphalerite.

Table 3 In situ lead isotopic compositions of sulfides from the Chalukou porphyry Mo deposit

No.	Sample No.	Depth (m)	Description	Mineral	$^{206}\text{Pb}/^{204}\text{Pb}$	1 σ	$^{207}\text{Pb}/^{204}\text{Pb}$	1 σ	$^{208}\text{Pb}/^{204}\text{Pb}$	1 σ
1	16CLK-26-1-1	380	Py-Fl and Qz-Py-Mol veins	Py-III	18.319	0.008	15.552	0.007	38.171	0.019
2	16CLK-26-1-2	380	Py-Fl and Qz-Py-Mol veins	Py-III	18.312	0.006	15.541	0.006	38.146	0.015
3	16CLK-26-2-2	380	Py-Fl and Qz-Py-Mol veins	Mol-I	18.370	0.007	15.570	0.006	38.218	0.015
4	16CLK-27-1-1	380	Mol-Py vein	Py-II	18.366	0.007	15.574	0.006	38.222	0.016
5	16CLK-27-1-3	380	Mol-Py vein	Mol-II	18.364	0.006	15.563	0.006	38.190	0.014
6	16CLK-27-1-4	380	Mol-Py vein	Mol-II	18.367	0.002	15.566	0.003	38.201	0.007
7	16CLK-27-1-5	380	Mol-Py vein	Mol-II	18.356	0.002	15.569	0.002	38.211	0.005
8	16CLK-27-2-1	380	Mol-Py vein	Py-II	18.365	0.007	15.559	0.007	38.180	0.017
9	16CLK-27-2-6	380	Mol-Py vein	Mol-II	18.347	0.017	15.550	0.018	38.153	0.049
10	16CLK-27-2-7	380	Mol-Py vein	Mol-II	18.364	0.006	15.576	0.007	38.226	0.018
11	16CLK-27-2-8	380	Mol-Py vein	Mol-II	18.386	0.009	15.597	0.009	38.282	0.023
12	16CLK-35-1-1	335	Qz-Py-Fl vein	Gn	18.338	0.007	15.569	0.007	38.206	0.020
13	16CLK-35-1-2	335	Qz-Py-Fl vein	Gn	18.335	0.007	15.566	0.007	38.196	0.020
14	16CLK-35-1-3	335	Qz-Py-Fl vein	Gn	18.336	0.007	15.568	0.007	38.200	0.020
15	16CLK-154-1-1	320	Py with minor Sp-Gn	Py-III	18.364	0.008	15.587	0.007	38.308	0.018
16	16CLK-154-1-2	320	Py with minor Sp-Gn	Mol-II	18.349	0.001	15.573	0.002	38.267	0.283
17	16CLK-154-2-2	320	Py with minor Sp-Gn	Sp	18.274	0.013	15.518	0.011	38.113	0.029
18	16CLK-154-3-1	320	Py with minor Sp-Gn	Py-III	18.312	0.005	15.542	0.006	38.180	0.023
19	16CLK-154-3-3	320	Py with minor Sp-Gn	Gn	18.346	0.007	15.573	0.007	38.258	0.019
20	16CLK-154-3-6	320	Py with minor Sp-Gn	Sp	18.278	0.015	15.518	0.015	38.099	0.039
21	16CLK-154-3-7	320	Py with minor Sp-Gn	Sp	18.310	0.006	15.535	0.006	38.097	0.018

Abbreviations: Fl = fluorite, Gn = galena, Mol = molybdenite, Py = pyrite, Qz = quartz, Sp = sphalerite.

Table 4 Whole rock lead isotopic compositions of intrusions from the Chalukou porphyry Mo deposit

No.	Sample No.	Depth (m)	Rock	$^{206}\text{Pb}/^{204}\text{Pb}$	1 σ	$^{207}\text{Pb}/^{204}\text{Pb}$	1 σ	$^{208}\text{Pb}/^{204}\text{Pb}$	1 σ
1	16CLK-69	985	fine-grained porphyry	18.479	0.002	15.559	0.002	38.336	0.006
2	16CLK-88	443	quartz porphyry	18.442	0.002	15.561	0.002	38.323	0.005
3	16CLK-130	627	granite porphyry	18.544	0.002	15.549	0.002	38.342	0.004
4	16CLK-136	1185	fine-grained porphyry	18.570	0.002	15.591	0.002	38.482	0.007

Fig. 1

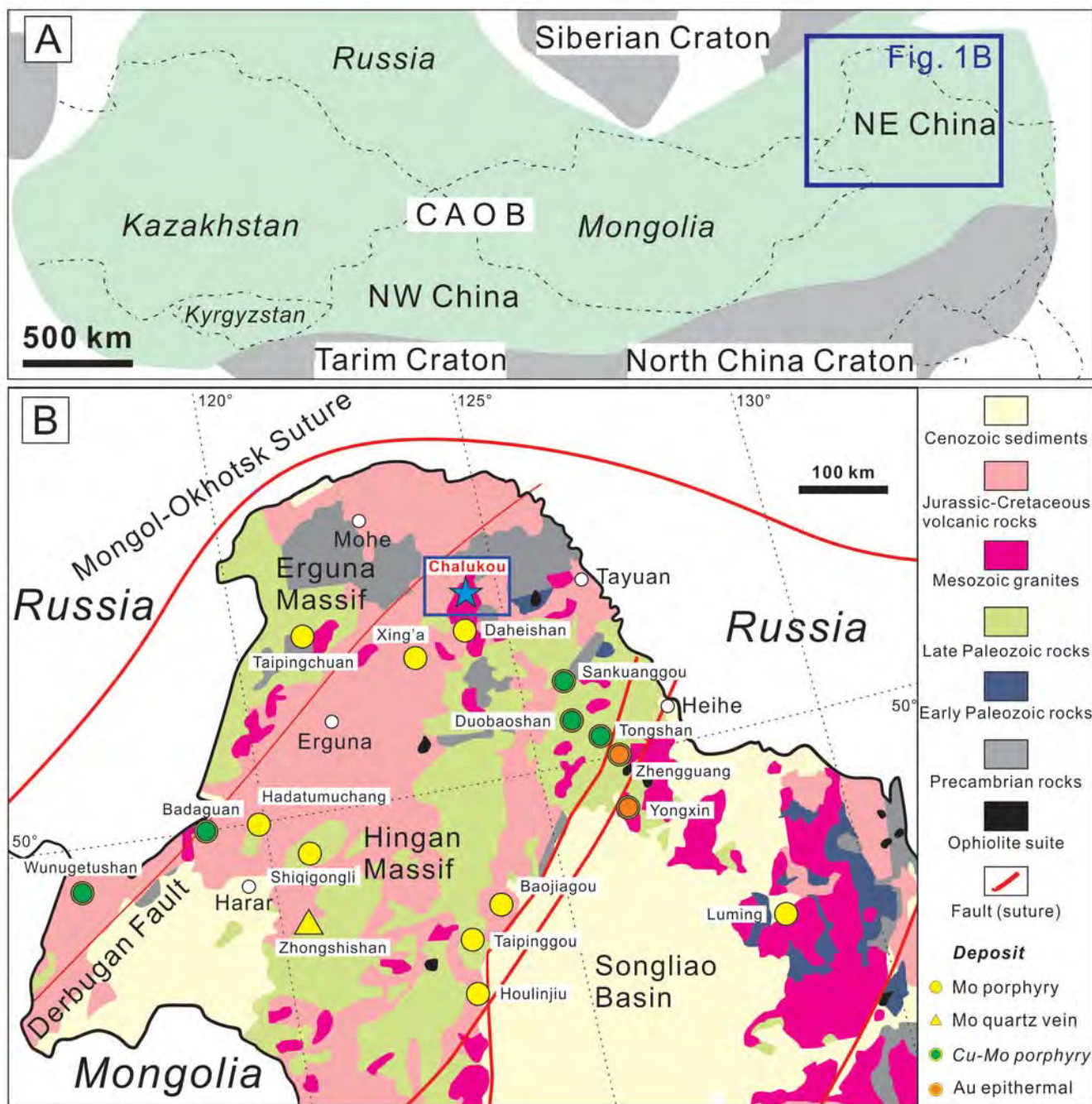
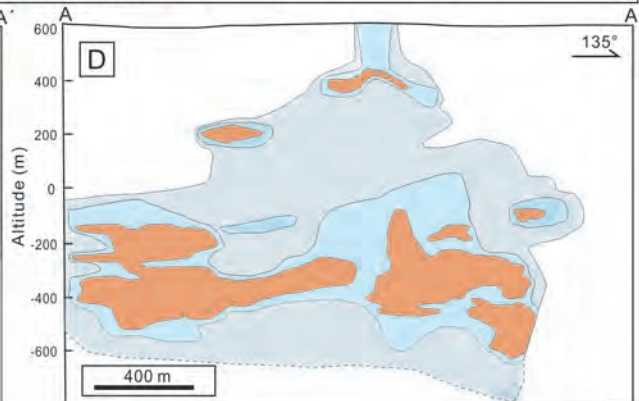
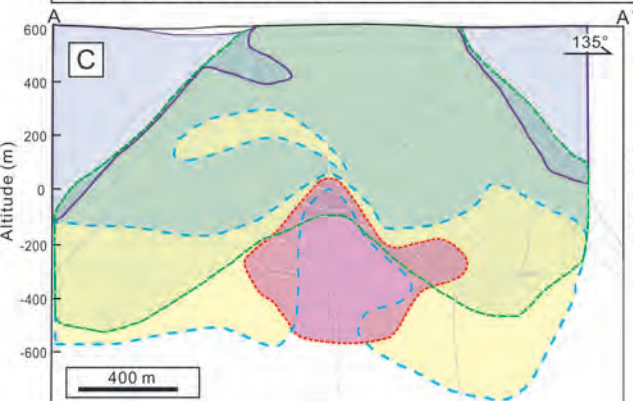
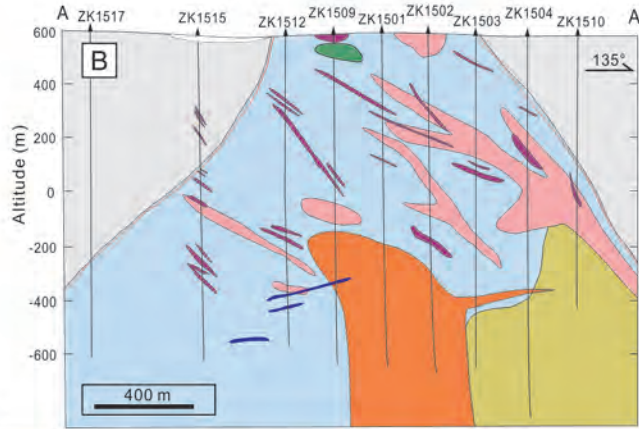
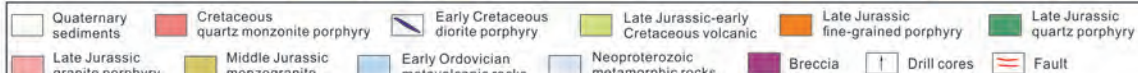
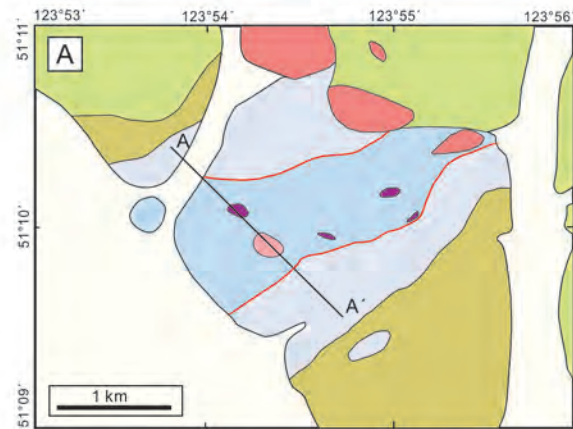


Fig. 2



Hydrothermal alteration zone

Silicic Potassic Phyllic and argillic Propylitic

Mo grade (wt.%)

Mo > 0.08 Mo > 0.06 Mo > 0.03 Mo < 0.03

Fig. 3

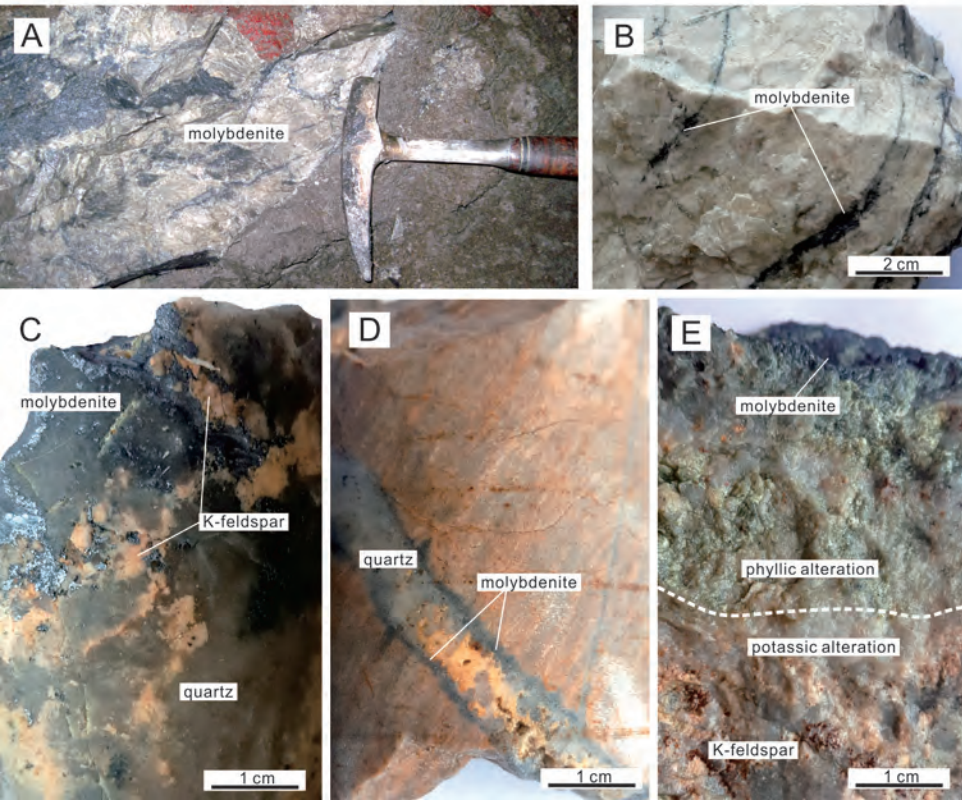


Fig. 4

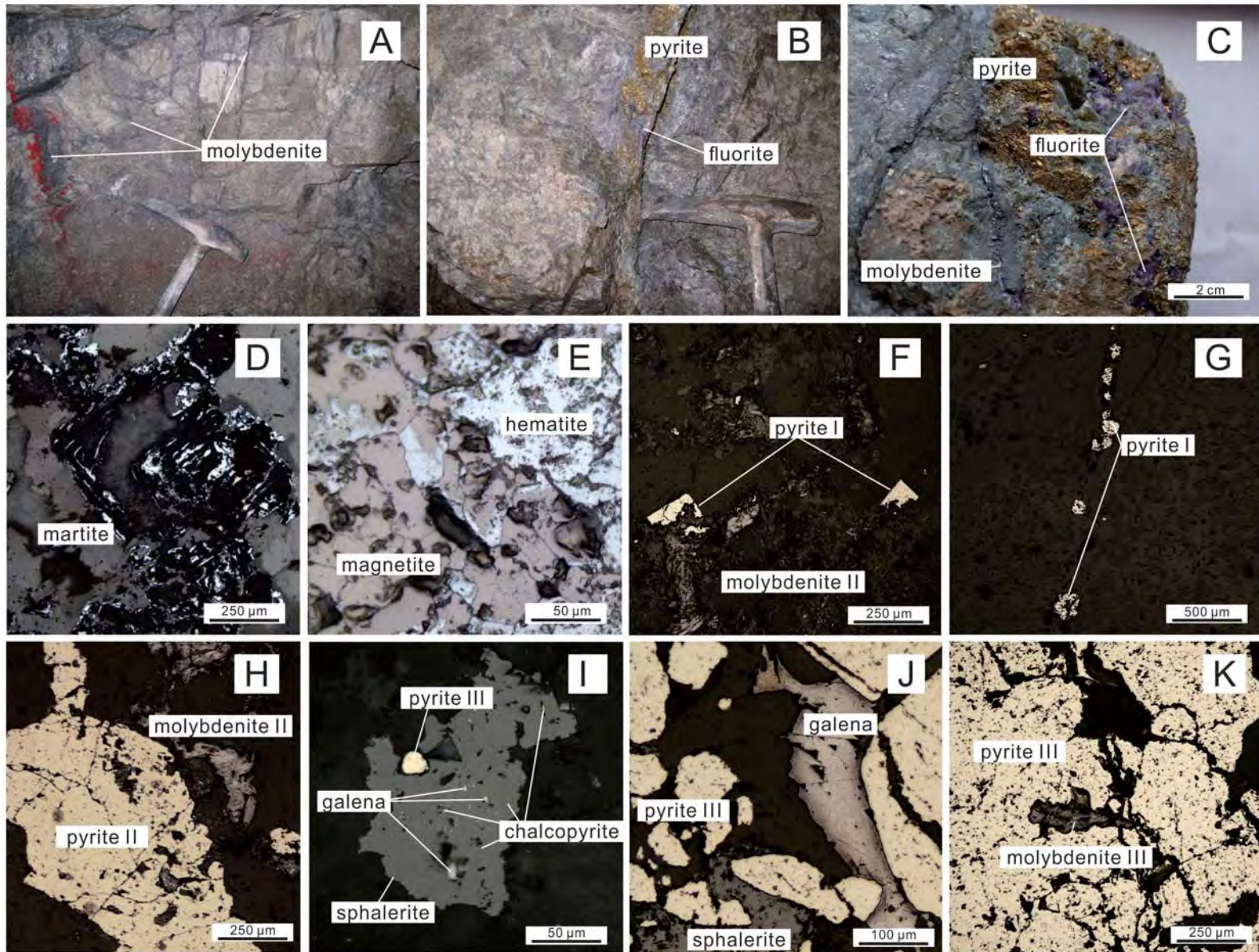


Fig. 5

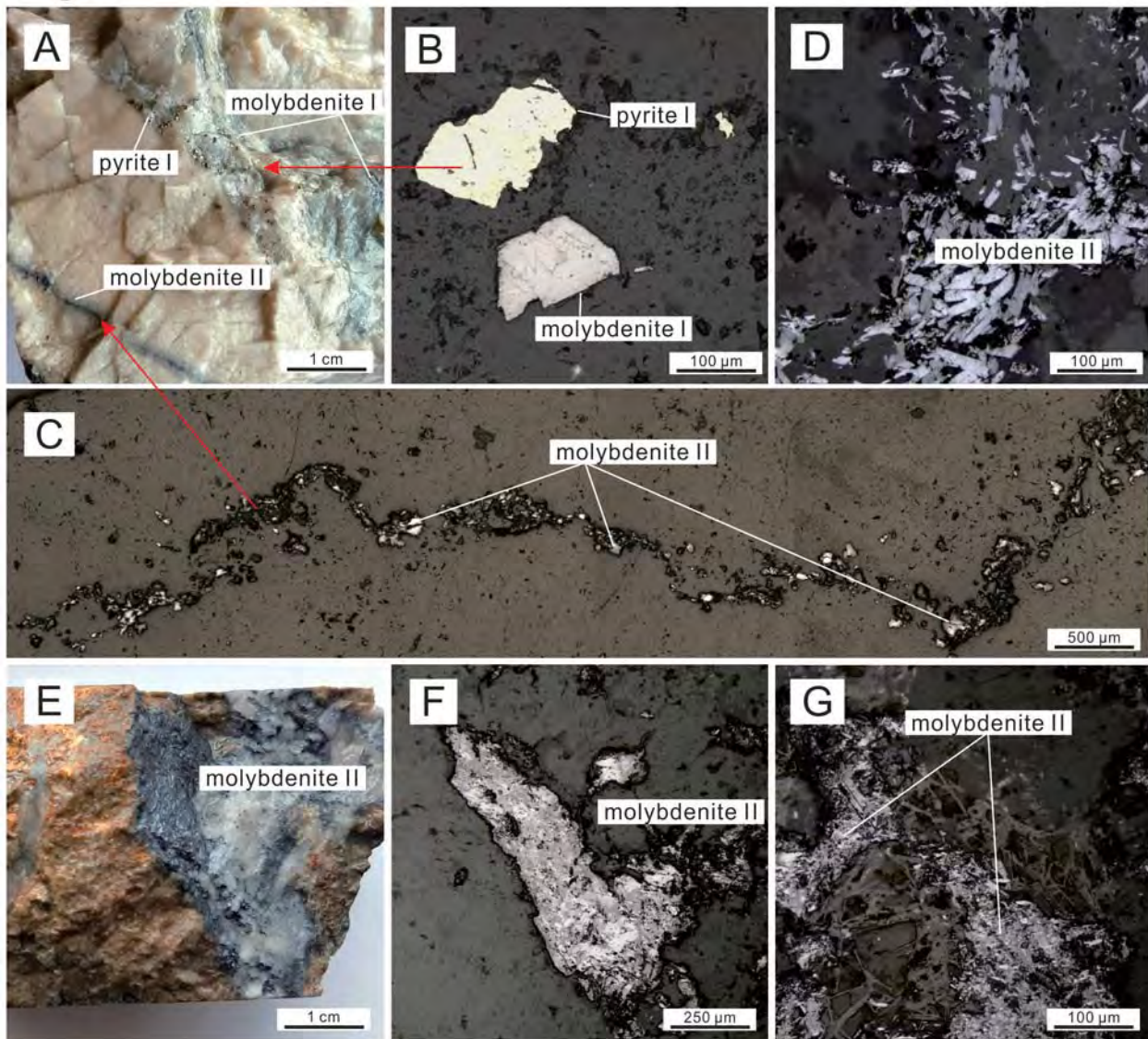


Fig. 6

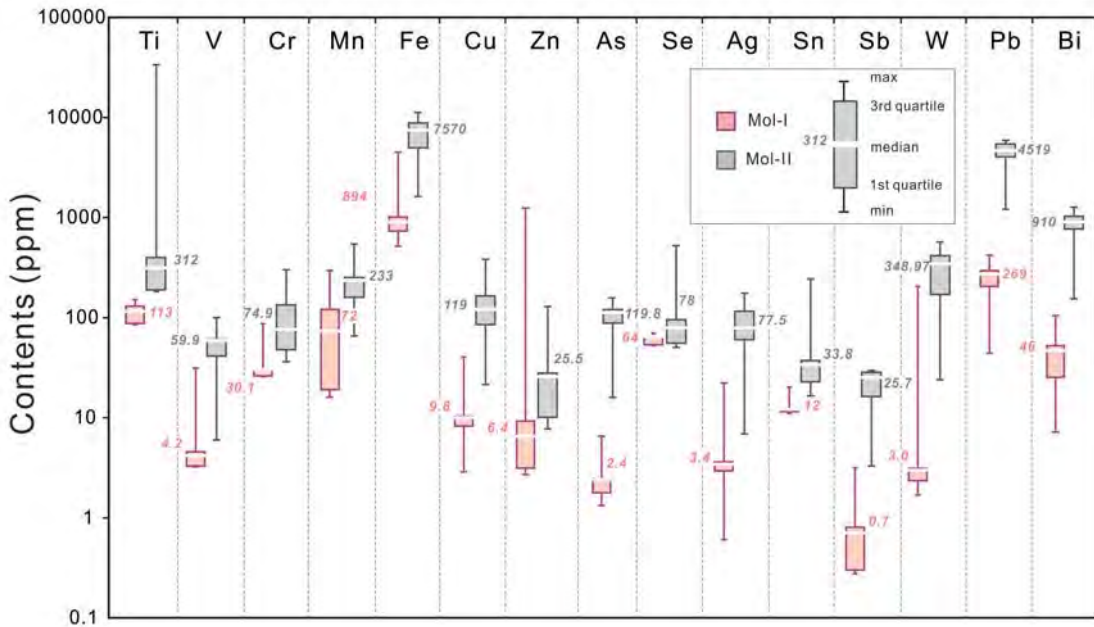


Fig. 7

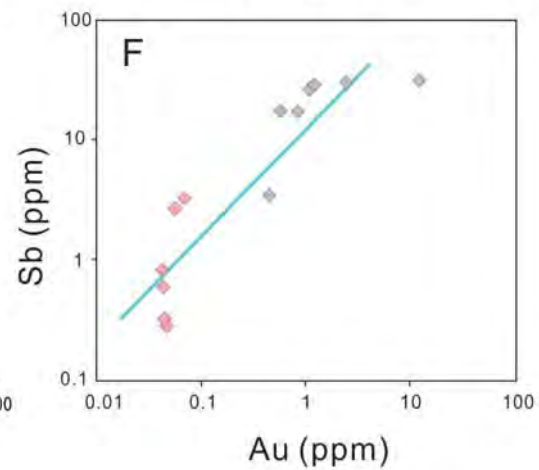
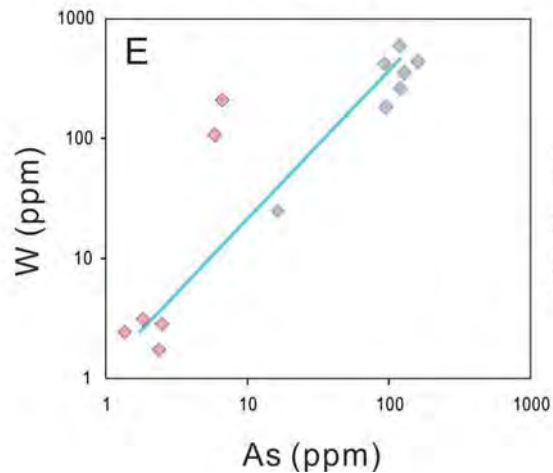
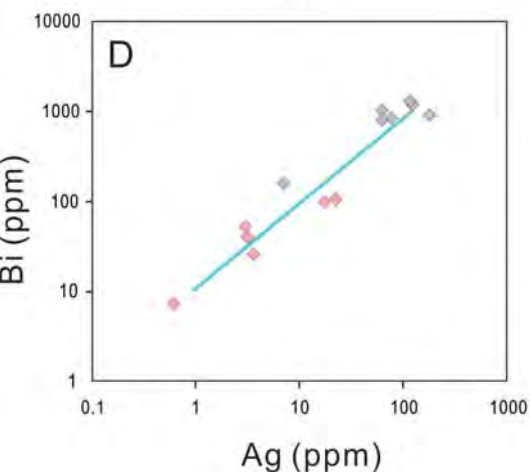
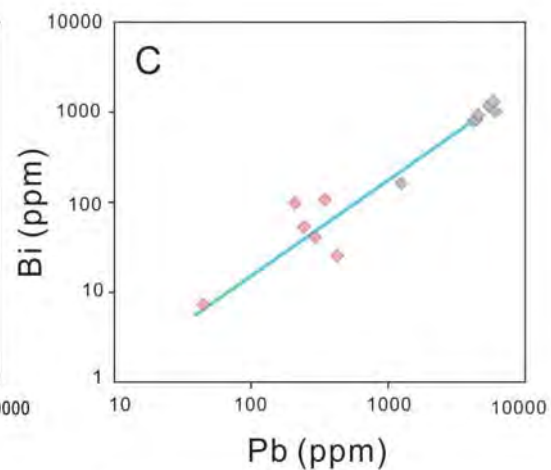
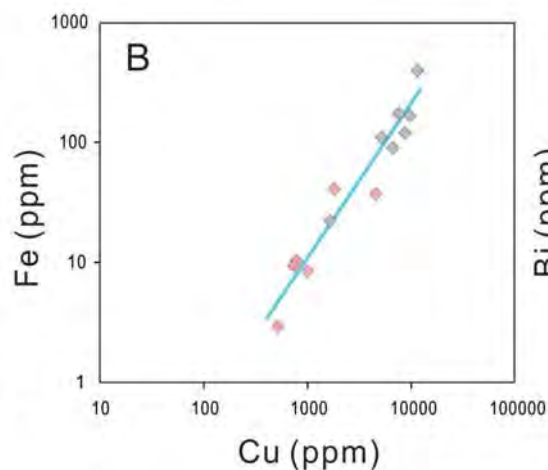
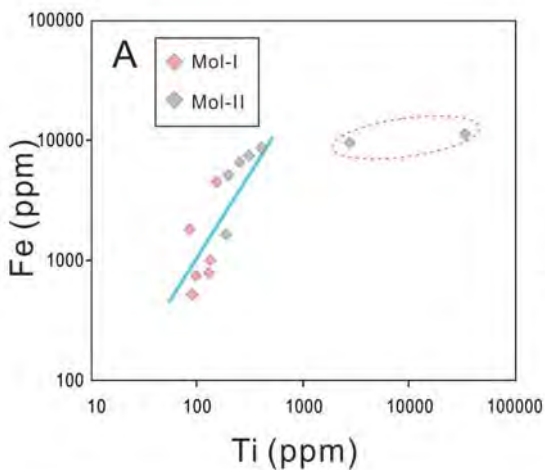


Fig. 8

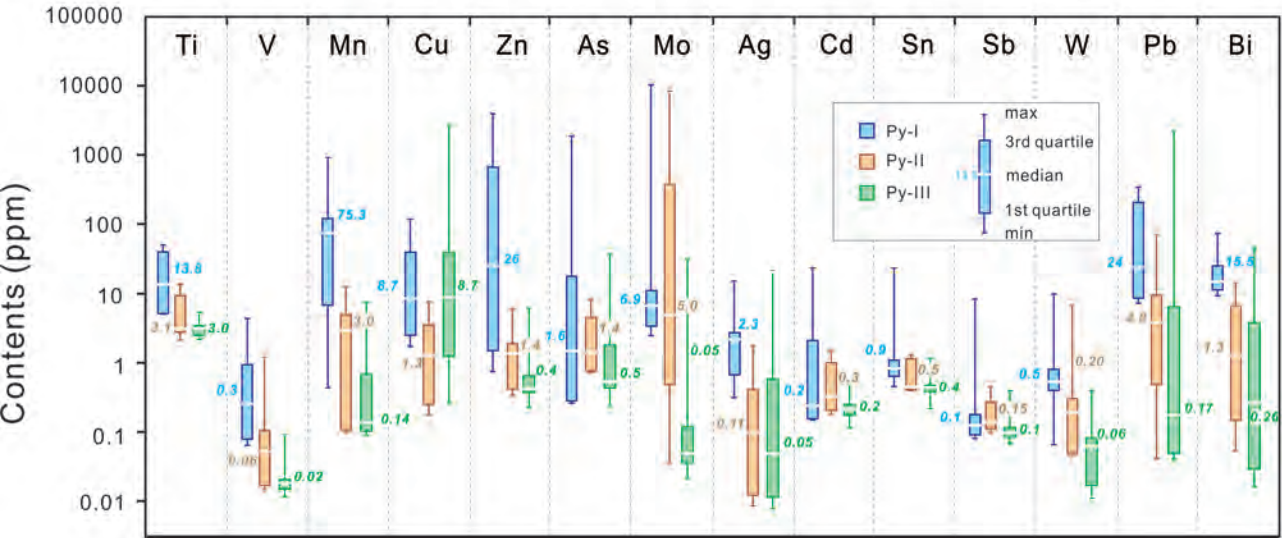


Fig. 9

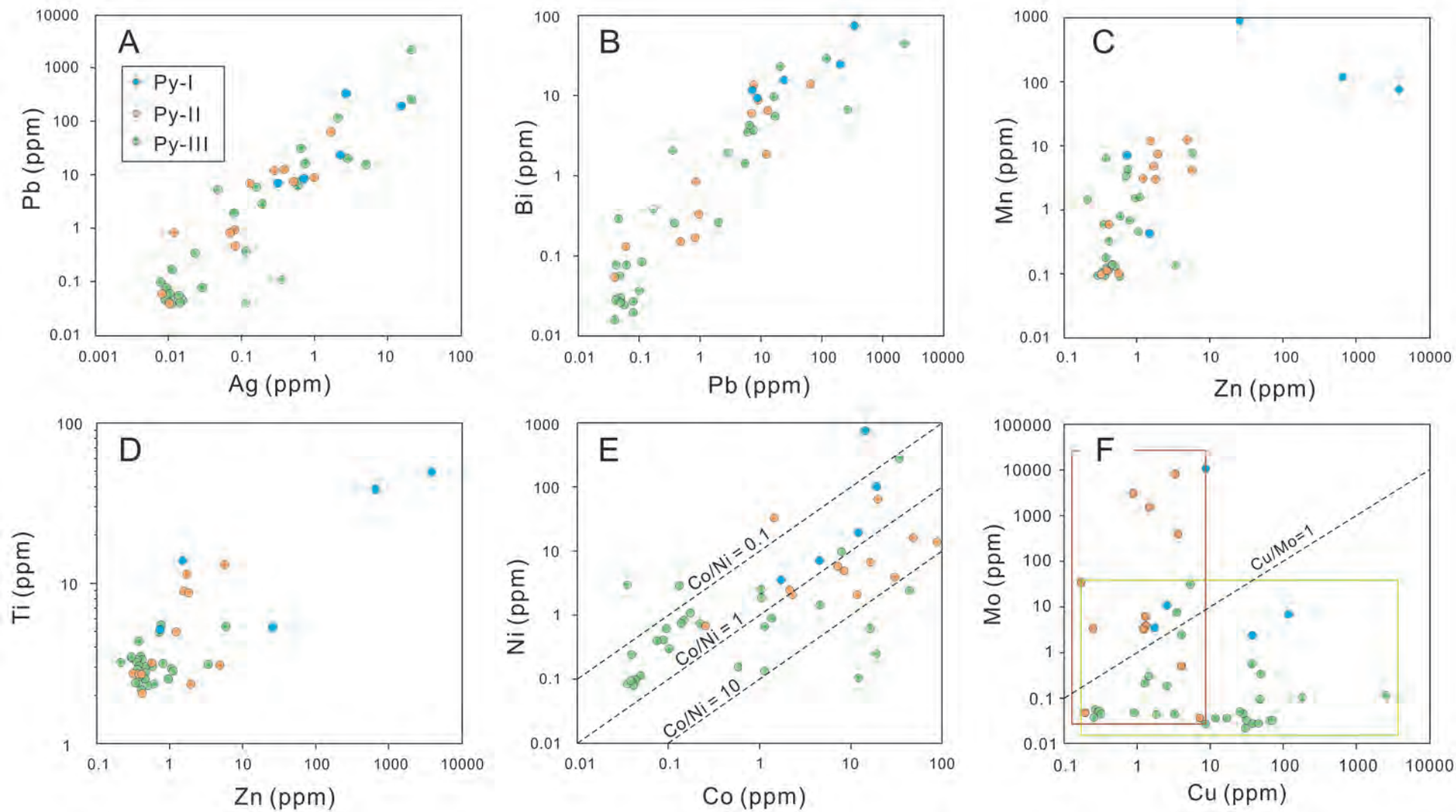
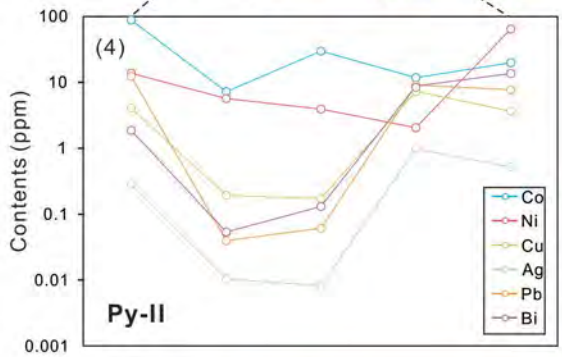
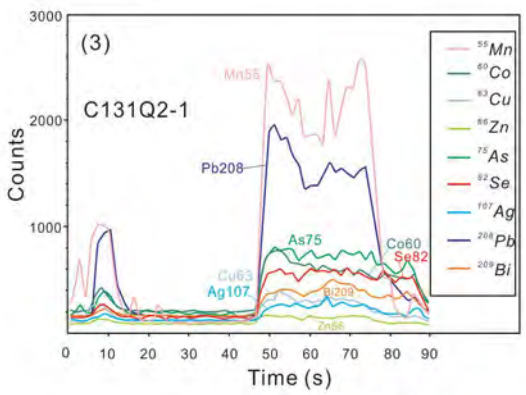
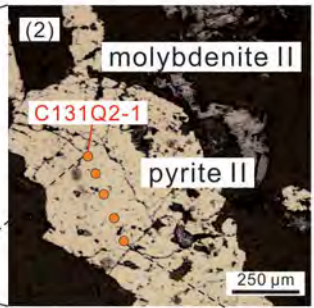
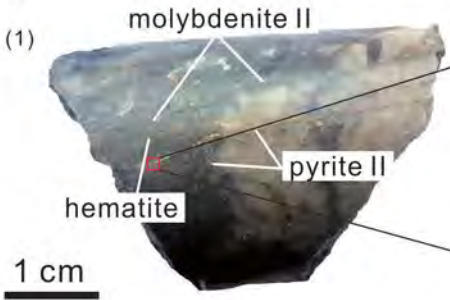


Fig. 10

A



B

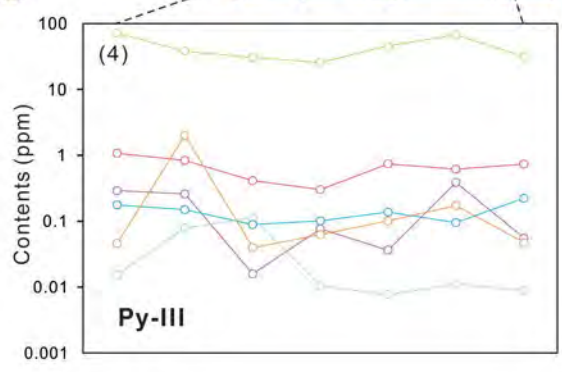
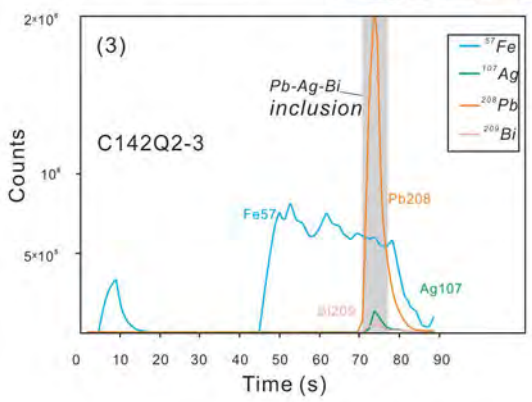
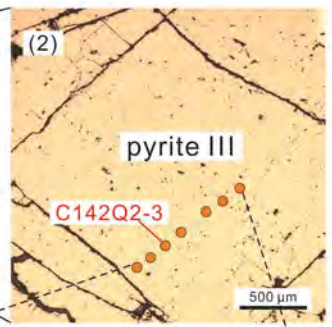
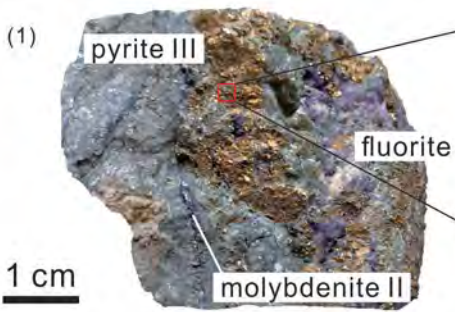


Fig. 11

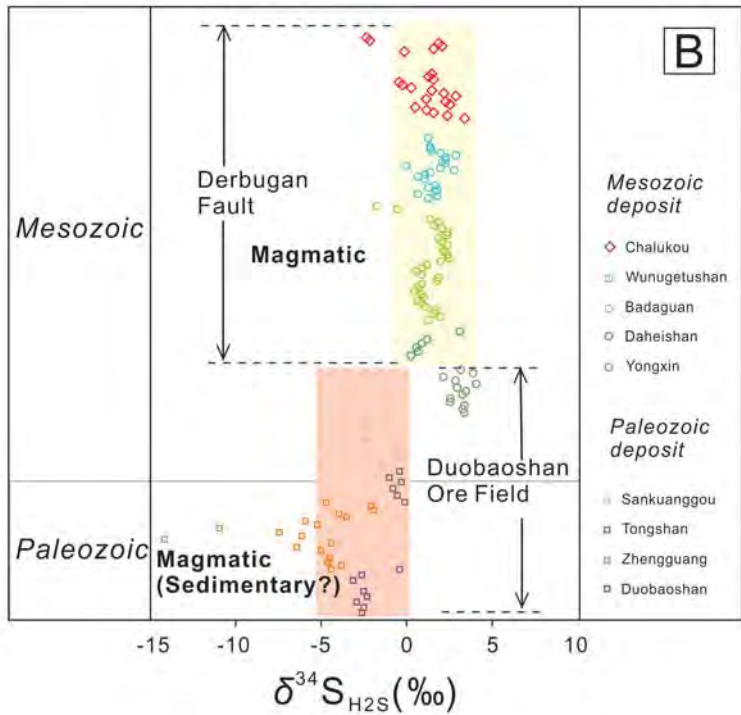
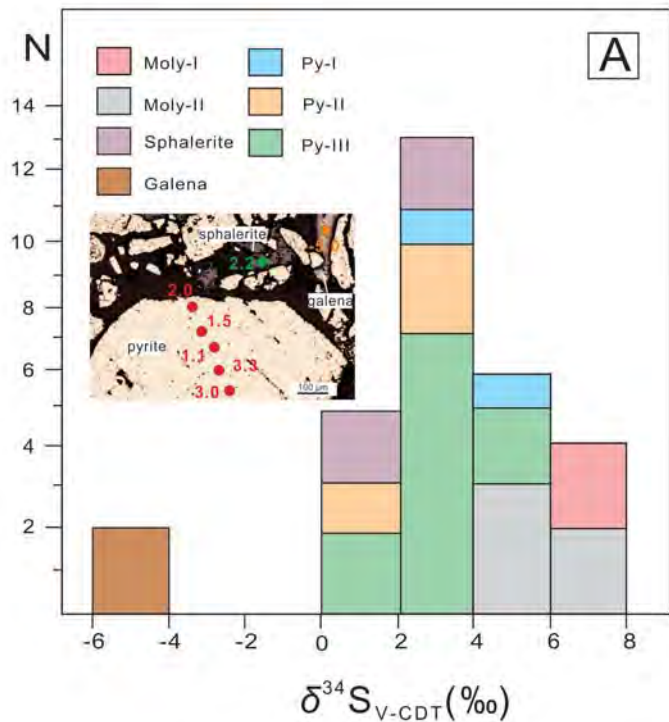


Fig. 12

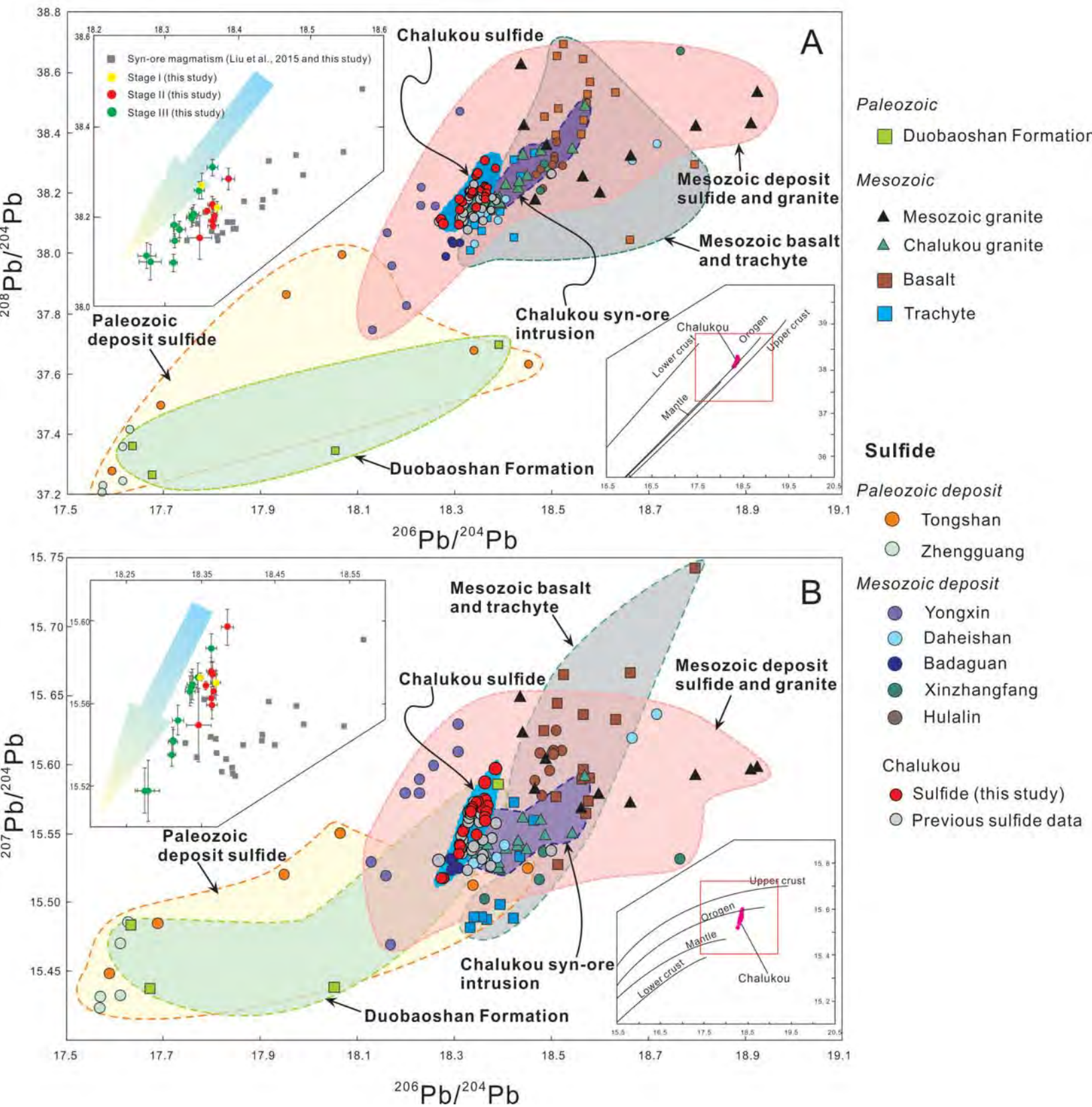


Fig. 13

